Hydrol. Earth Syst. Sci. Discuss., 11, 8443–8492, 2014
www.hydrol-earth-syst-sci-discuss.net/11/8443/2014/
doi:10.5194/hessd-11-8443-2014

Hydrology and Earth System Sciences
Open Access
Discussions

Resolving terrestrial ecosystem processes along a subgrid topographic gradient for an earth-system model

Z. M. Subin[1,2], **P. C. D. Milly**[3,2], **B. N. Sulman**[2,4], **S. Malyshev**[1,2], **and E. Shevliakova**[1,2]

[1]Princeton Environmental Institute, Princeton University, Princeton, New Jersey, USA
[2]Geophysical Fluid Dynamics Laboratory, National Oceanic and Atmospheric Administration, Princeton, New Jersey, USA
[3]US Geological Survey, Princeton, New Jersey, USA
[4]School of Public and Environmental Affairs, Indiana University, Bloomington, Indiana, USA

Received: 29 May 2014 – Accepted: 1 July 2014 – Published: 23 July 2014

Correspondence to: Z. M. Subin (subin@post.harvard.edu)

Published by Copernicus Publications on behalf of the European Geosciences Union.

Abstract

Soil moisture is a crucial control on surface water and energy fluxes, vegetation, and soil carbon cycling. Earth-system models (ESMs) generally represent an areal-average soil-moisture state in gridcells at scales of 50–200 km and as a result are not able to capture the nonlinear effects of topographically-controlled subgrid heterogeneity in soil moisture, in particular where wetlands are present. We addressed this deficiency by building a subgrid representation of hillslope-scale topographic gradients, TiHy (Tiled-hillslope Hydrology), into the Geophysical Fluid Dynamics Laboratory (GFDL) land model (LM3). LM3-TiHy models one or more representative hillslope geometries for each gridcell by discretizing them into land model tiles hydrologically coupled along an upland-to-lowland gradient. Each tile has its own surface fluxes, vegetation, and vertically-resolved state variables for soil physics and biogeochemistry. LM3-TiHy simulates a gradient in soil moisture and water-table depth between uplands and lowlands in each gridcell. Three hillslope hydrological regimes appear in non-permafrost regions in the model: wet and poorly-drained, wet and well-drained, and dry; with large, small, and zero wetland area predicted, respectively. Compared to the untiled LM3 in stand-alone experiments, LM3-TiHy simulates similar surface energy and water fluxes in the gridcell-mean. However, in marginally wet regions around the globe, LM3-TiHy simulates shallow groundwater in lowlands, leading to higher evapotranspiration, lower surface temperature, and higher leaf area compared to uplands in the same gridcells. Moreover, more than four-fold larger soil carbon concentrations are simulated globally in lowlands as compared with uplands. We compared water-table depths to those simulated by a recent global model-observational synthesis, and we compared wetland and inundated areas diagnosed from the model to observational datasets. The comparisons demonstrate that LM3-TiHy has the capability to represent some of the controls of these hydrological variables, but also that improvement in parameterization and input datasets are needed for more realistic simulations. We found large sensitivity in

HESSD
11, 8443–8492, 2014

model-diagnosed wetland and inundated area to the depth of conductive soil and the parameterization of macroporosity. With improved parameterization and inclusion of peatland biogeochemical processes, the model could provide a new approach to investigating the vulnerability of Boreal peatland carbon to climate change in ESMs.

1 Introduction

Earth-system models (ESMs) are increasingly used to evaluate terrestrial biogeochemical feedbacks to climate change (Ciais et al., 2013). Disturbance of the carbon cycle in natural ecosystems by changing climate could cause a positive feedback to climate change by increasing mineralization of currently stable soil-carbon pools (Grosse et al., 2011; Schuur et al., 2008). However, the horizontal length scale at which these ecosystems vary in their vulnerability to changes in temperature or wetness is much smaller than the scale resolved by the land-model grid in ESMs. In particular, small-scale variations in hydrology affect surface fluxes, vegetation, and soil biogeochemical cycling by modulating soil moisture, with mean characteristics poorly estimated by assuming the mean soil moisture state (Nykanen and Foufoula-Georgiou, 2001; Wood et al., 2011). In many ecosystems, groundwater is responsible for maintaining vegetation during dry spells and providing a source of water for wetlands. Hydrological variations at spatial scales of ~ 1 km or less can be very important for larger-scale biogeochemistry. For example, a large fraction of primary productivity and biomass in arid and semiarid regions can be concentrated in small areas of water convergence such as streambeds (e.g., Kassas, 1952). In wet regions, peatlands covering a small fraction of total land area can account for a disproportionately high fraction of total soil carbon (Buffam et al., 2011; Weishampel et al., 2009). Northern peatlands contain 400–600 Pg of soil carbon (Yu, 2012) but are poorly represented in current ESMs and terrestrial ecosystem models, partially because these models cannot represent hydrology at the fine scales relevant to peatland formation (Frolking et al., 2009; Sulman et al., 2012); a number of syntheses

HESSD
11, 8443–8492, 2014

have highlighted the importance of improving the representation of peatlands in ESMs in order to better estimate their vulnerability to climate change (Frolking et al., 2011; Limpens et al., 2008). Wetlands are also the dominant source of natural methane emissions, which have highly nonlinear responses to variations in hydrology (Walter and Heimann, 2000). In addition to their role in the carbon cycle, wetlands and other small-scale hydrological features provide important ecosystem services such as wildlife habitat and water-quality enhancement, and hydrological representation at appropriate scales will be necessary for simulating future changes in wetland area.

ESMs participating in the Coupled Model Intercomparison Project Phase 5 (CMIP5) had land grid spacing no smaller than $\sim 1^{\circ}$ (Todd-Brown et al., 2013). Some current ESMs contain aboveground subgrid heterogeneity in vegetation (e.g., Lawrence et al., 2011) or belowground subgrid heterogeneity among managed ecosystems (Shevliakova et al., 2009), but none model belowground subgrid heterogeneity in natural ecosystems. Consequently, advances in ESM formulation are needed to represent the subgrid-scale hydrological processes that govern the distinct biogeochemistry of ecosystems like peatlands.

At least a simple formulation of groundwater dynamics is increasingly being incorporated into climate models (Gulden et al., 2007; Krakauer et al., 2013; Milly and Shmakin, 2002; Miguez-Macho et al., 2007; Niu et al., 2007), with improved simulation of runoff and evapotranspiration (ET) commonly resulting (Campoy et al., 2013; Choi and Liang, 2010; Leung et al., 2011; Vergnes et al., 2012; Koirala et al., 2013; Vergnes and Decharme, 2012). Groundwater processes can even cause simulated changes in large-scale precipitation (Lo and Famiglietti, 2011; Yuan et al., 2008). However, current ESM groundwater treatments are limited in that only areal-mean groundwater and soil states are modelled for each gridcell (except for models considering variation due to land use), preventing treatment of a hydrologic gradient within the gridcell. Because the spatial scale of groundwater processes controlling wetland formation is significantly smaller than a gridcell, sub-grid-scale variation in hydrology is necessary to model the

HESSD
11, 8443–8492, 2014

nonlinear effects of soil moisture on soil carbon cycling and methane emissions (e.g., Bohn and Lettenmaier, 2010; Zhu et al., 2014).

Several approaches have been used to address the challenge of modelling the effects of subgrid variability in groundwater depth, but these existing approaches suffer from several limitations. TopModel (Beven and Kirkby, 1979) can be used to diagnose wetland area or methane emissions based on the gridcell-mean water-table depth and the local topographic distribution (Riley et al., 2011; Ringeval et al., 2010, 2012; Merot et al., 2003; Kleinen et al., 2012; Schuldt et al., 2013). TopModel is limited by assumptions about the temporal and geographic variation of the water table (Fan and Miguez-Macho, 2011) and may under-predict wetlands in flat areas where wetlands would be prominent (Stacke and Hagemann, 2012). Moreover, using TopModel to predict saturated area for methane emissions without modelling unsaturated wetlands may produce biases in simulated emissions (Bohn et al., 2013). Stacke and Hagemann (2012) formulated a global dynamic wetland model without the limiting assumptions of TopModel, but did not model separate soil and vegetation states along a gradient from upland to wetland. Bohn et al. (2013) used a regionally calibrated model to simulate the effects of fine-scale heterogeneity in water-table depth on methane emissions, but have not extended this approach to global scales. An alternative approach is to couple a comprehensive three-dimensional (3-D) groundwater model into the land component of a climate model (Choi et al., 2007; Maxwell et al., 2011; Pan et al., 2008; Rihani et al., 2010; Shen and Phanikumar, 2010; Tian et al., 2012; Xie et al., 2012). Such an approach requires high resolution and is thus computationally expensive and requires extensive input data, and thus may not be practical for modelling wetland dynamics at a global scale.

Explicitly considering hydrology along a typical hillslope gradient provides another avenue for incorporating subgrid hydrological heterogeneity into global models. Landscapes can be conceptualized as the union of fundamental hillslope units (Winter, 2001), including valleys and plains as relatively flat hillslopes. Hillslopes can be categorized into characteristic shapes for determining their hydrology (Troch

HESSD
11, 8443–8492, 2014

et al., 2003). The hillslope length scale (∼ 1 km) captures groundwater dynamics on a timescale of days to years and is the scale at which lateral flows represent a significant proportion of the hydrologic budget (Krakauer et al., 2014). Incorporating hillslope-scale dynamics into an ESM can inform estimates of runoff and saturated fraction (Milly et al., 2014). A two-dimensional (2-D) representation of groundwater flows within the hillslope, with a vertical dimension and one horizontal dimension following the downslope gradient, can be used to approximate the 3-D flow field (Hilberts et al., 2007; Paniconi et al., 2003). Hillslope-scale heterogeneity can affect ET and vegetation properties (Atchley and Maxwell, 2011); for example, groundwater convergence increases leaf area index (LAI) in valley bottoms as compared with hilltops in some regions (e.g., O'Grady et al., 2011).

A recent synthesis provided a framework for incorporating groundwater hydrology and wetland dynamics into ESM-compatible land models (Fan and Miguez-Macho, 2011). In this study, we introduce a representation of hillslope-scale groundwater dynamics into such a land model: this represents a step towards the comprehensive approach outlined in Fan and Miguez-Macho (2011). By discretizing the representation of ecosystems along the hillslope gradient from upland to lowland in each land model gridcell, we aim to simulate heterogeneity in surface fluxes, vegetation properties, and soil biogeochemical cycling due to variations in soil moisture along the hillslope. This allows the mechanistic simulation of the hydrologic controls of groundwater-fed wetland dynamics, with a variable wetland area simulated as a changing number of discretized ecosystem units experience a near-surface water table. In a computationally efficient way (i.e., without need for a comprehensive, high-resolution 3-D groundwater model), the new model is intended to provide a bridge between the ecosystem plot scale where surface fluxes occur, modulated by soil moisture heterogeneity, and the land-model-resolved grid scale. This represents an extension of the aboveground ecosystem patch concept (Bonan et al., 2002) in which representative ecosystem types are scaled by their respective areas to determine the mean gridcell fluxes to the atmosphere. With

HESSD
11, 8443–8492, 2014

this extension, topographic position is now a characteristic of each patch, and patches interact via groundwater flow.

2 Methods

2.1 Land model with parameterization of lateral flow: LM3

The model serving as our starting point was the Geophysical Fluid Dynamics Laboratory (GFDL) Land Model 3 (LM3), which is routinely coupled into the GFDL ESM. LM3 (Shevliakova et al., 2009; Milly et al., 2014) consists of a model from canopy air down to impermeable bedrock of: bidirectional diffuse and direct, visible and near-infrared radiation transfer; photosynthesis and stomatal conductance; surface energy, momentum, and water fluxes; snow physics; soil thermal and hydraulic physics (including advection of heat by water fluxes); vegetation phenology, growth, and mortality; simple plant-functional-type-transition dynamics; simple soil-carbon dynamics; and representation of lakes, glaciers, and the river network. LM3 includes an extensive treatment of anthropogenic land-cover change, with the capability to represent conversion among cropland, pasture, natural vegetation, and secondary vegetation, but it does not at present include irrigation, groundwater pumping, or intentional drainage of wetlands. Rooting depths and soil-moisture limitation on photosynthesis are important parameters for determining the effects of soil moisture on vegetation. Root fractions decay exponentially from the surface with e-folding depths for the LM3 species (Shevliakova et al., 2009) ranging from 0.17 to 0.35 m (Jackson et al., 1996, 1997). As described in Milly et al. (2014), xylem, root, and soil resistances to transpiration downregulate stomatal conductance under conditions of low soil moisture and high vapour-pressure deficit.

One feature of LM3 is a flexible tiling scheme that allows a variable number of land-model tiles to be modelled in each gridcell, with the number of tiles in each gridcell changing as tiles are created or merged throughout the simulation (Shevliakova

HESSD
11, 8443–8492, 2014

et al., 2009). Each tile has its own surface fluxes and state variables for vegetation and soil. This tiling has been crucial in the mechanistic investigation of the effects of anthropogenic land cover change (Shevliakova et al., 2009; Gerber et al., 2013) but has not been used to simulate subgrid heterogeneity in natural, undisturbed ecosystems. Here, we exploit the flexible tiling scheme to introduce a hillslope dimension into natural ecosystems (Sect. 2.2).

The version of LM3 described in Milly et al. (2014) combines a columnar representation of 1-D physics with a parameterization of the lateral flow based on an idealized hillslope unit. The 1-D conservation equation for liquid water is:

$$\frac{\partial \theta}{\partial t} = -\frac{\partial q}{\partial z} - r - G + M - \phi, \tag{1}$$

where t [s] is time, z [m] is the vertical coordinate, θ [–] is the soil water content, r [s^{-1}] is the root uptake, G [s^{-1}] is the lateral groundwater divergence, M [s^{-1}] is the absorption from macropores, ϕ [s^{-1}] is the freezing rate, and q is the vertical water flux, determined by Darcy's Law. The domain is vertically discretized into layers down to an impermeable base B. In determining q and G, the saturated hydraulic conductivity K [$m\,s^{-1}$] of the porous matrix follows an exponential profile (e.g., Beven and Kirkby, 1979) between the relatively conductive soil and the usually less conductive bedrock or unconsolidated material below the soil, henceforth referred to simply as "bedrock":

$$K = K_s \exp\left\{-\frac{d}{z_s}\right\} + K_B\left(1 - \exp\left\{-\frac{d}{z_s}\right\}\right), \tag{2}$$

where d is the depth below the local surface, z_s is a soil depth-scale, K_s is the saturated soil conductivity, and K_B is the saturated conductivity of the bedrock. K_s is based partially on soil texture, but also includes a contribution from macroporosity K_m [$m\,s^{-1}$] under saturated conditions (Milly et al., 2014). In addition to the groundwater table modelled by LM3, a reduction of hydraulic conductivity in frozen soils allows for the modelling of a perched water table in permafrost areas.

HESSD
11, 8443–8492, 2014

Of special interest here is the parameterization of G, which is a pre-determined function of the water-table depth and hillslope geometry. This function is derived under the assumption of steady-state, horizontal (1-D) groundwater flow, to (but not from) a fully penetrating stream, within an idealized hillslope unit. The hillslope unit (Fig. 1a) consists of a 2-D hillslope profile having a vertical dimension z and a horizontal dimension x parallel to the downslope gradient, with a width $w(x)$ perpendicular to the resolved downslope dimension x. Water generally flows downslope from $x = L$ (the hillslope length) to the stream at $x = 0$. The shapes of the surface elevation profile $Z(x)$ and the width $w(x)$ are flexible, to be based on topographic properties in each land model gridcell, which can contain more than one representative hillslope. General 3-D hillslopes with surfaces not flat along the dimension perpendicular to x can be approximated in this 2-D formulation by transforming the variable area at a given elevation Z into a variable width along x.

2.2 Hillslope discretization: LM3-TiHy

The model presented here is denoted as LM3-TiHy (Tiled-hillslope Hydrology). Its fundamental innovation is the use of multiple soil tiles along the hillslope to explicitly resolve horizontal variation associated with hillslope-scale hydrology (Fig. 1b). Each tile is governed by Eq. (1), but G is now evaluated directly by application of Darcy's Law laterally between tiles to generate a 2-D water flow field (Fig. 2). This 2-D field is determined using a variably-saturated hydraulic formulation that allows for fluxes both vertically and horizontally in both saturated and unsaturated zones. This approach removes the inherent steady-state groundwater assumption used by Milly et al. (2014) and permits explicit tracking of soil hydraulic, thermal, and biogeochemical states along the topographic gradient.

Here, the horizontal Darcy's Law yields:

$$G(x,z) = -\frac{\partial}{\partial x}\left[K\frac{\partial h}{\partial x}\right], \tag{3}$$

HESSD
11, 8443–8492, 2014

where $h = \psi + z$ [m] is the total hydraulic head. The coupled system of equations describing the 2-D flow is solved by separating the slow horizontal inter-tile flows from the fast vertical intra-tile flows. The horizontal fluxes defining G are calculated explicitly and prescribed as vertically-discretized source or sink terms in the time-implicit solution of the vertical Richards equation (Milly et al., 2014), in which θ is updated. Complete details of the hillslope unit, its discretization, and the evaluation of the horizontal hydraulic fluxes are provided as a technical note in the Supplement. In the simplest case of equal-length tiles and a constant-width hillslope, G is discretized for each layer l and tile j as:

$$G_j(l) = \frac{\Delta z_l}{L_n^2}\left(\frac{\left[\widehat{K}_l \Delta h_l\right]_{j-1}}{a_{j-1}} + \frac{\left[\widehat{K}_l \Delta h_l\right]_{j+1}}{a_{j+1}}\right), \quad (4)$$

where $G_j(l)$ [m s^{-1}] is the sum of the water fluxes out of tile j into tiles $j-1$ and $j+1$ per unit area of tile j, Δz_l [m] is the thickness of layer l, L_n [m] is the hillslope length divided by the number of tiles, $\widehat{K}_l$ is the product of the harmonic-mean hydraulic conductivity [m s^{-1}] and the amount by which the hydraulic head in tile j exceeds that in the neighboring tiles for layer l, and $a = \frac{1}{L}\sqrt{(\Delta h)^2 + L^2}$ is a geometric factor.

The boundary condition for the hilltop tile ($x = L$), hereafter denoted as the "upland," is zero flux; while the boundary condition for the bottom tile ($x = 0$), hereafter denoted as the "lowland", is a stream defined as a finite-depth channel with zero matric potential ψ at its surface and a hydrostatic potential below. The lowland communicates with the stream using the $j-1$ portion of Eq. (4), modified by a factor of 2 (as the distance to the stream is only $L_n/2$) and a conductivity scalar k_s [–]:

$$k_s(l) = \exp\left\{-\frac{d_l}{z_{str}}\right\}, \quad (5)$$

HESSD
11, 8443–8492, 2014

where d_l is the depth to the midpoint of layer l and $z_{str} = 1.5\,m$ is the stream depth. Surface runoff is parameterized as in Milly et al. (2014) and is assumed to flow downslope directly to the stream, bypassing the intervening tiles.

Greater wetland area, as simulated by the fractional area of tiles with a near-surface water table, should naturally occur in regions with low slope, low hydraulic conductivity, and greater net recharge. Each tile with a near-surface water table will have surface fluxes, vegetation, and soil biogeochemistry explicitly responsive to this wet soil-moisture state. Furthermore, as the real land surface of the gridcell is composed of a large number of repeating hillslope units of different geometries, this can be modelled by scaling up from one or more representative modelled hillslope units of varying geometries according to their respective area fractions.

2.3 Model implementation and datasets for parameterization

In the simulations conducted here, one or two characteristic hillslopes are discretized into 10 equal-length (in the x direction) tiles in each gridcell. The shape of the hillslope profile is assumed to be power-law according to:

$$Z(x) = \zeta L \left(\frac{x}{L}\right)^{\beta}, \tag{6}$$

where $\zeta > 0$ is a characteristic slope, and $\beta > 0$ determines whether the profile is convex ($\beta < 1$), linear ($\beta = 1$), or concave ($\beta > 1$). The slope width shape is linear:

$$w(x) = 1 + (W - 1)\frac{x}{L}, \tag{7}$$

where w is normalized to the width at the stream, and $W > 0$ is the ratio of the width at the hilltop to the width at the stream: $W < 1$ implies a diverging shape, $W = 1$ a parallel shape, and $W > 1$ a converging shape.

Hillslope-scale topography is an important input for TiHy, but no global dataset including such properties as hillslope shape and soil depth to bedrock currently exists.

HESSD
11, 8443–8492, 2014

We have used two datasets here for topographic slope to define ζ in the model (without further information about hillslope shape): one based on the Food and Agricultural Organization (FAO) soil database (FAO/UNESCO, 2003), and one based on the Harmonized World Soil Database (HWSD) (FAO/IIASA/ISRIC/ISSCAS/JRC, 2012). For the $1/12^{\circ}$ FAO dataset, we used the mean slope in each slope-range category and interpolated to determine the mean topographic slope in each land-model gridcell, as in Milly et al. (2014). For the HWSD dataset at $1/12^{\circ}$ resolution, we either used the mean slope, or we interpolated to find the 50th percentile slope in each land-model gridcell, defining one hillslope with the mean slope over the 0 to 50th percentile and one with the mean slope over the 50th to 100th percentile. This latter experiment (Sect. 2.4) was intended to more realistically represent areas with bimodal slope distribution, i.e., due to the presence of valleys contrasting with hills or mountains. Although the HWSD dataset is generally superior to FAO, it excludes land poleward of 60° latitude, so we filled in with the FAO data in this zone and chose the FAO dataset for our default simulations to avoid artifacts resulting from this discontinuity. We also note that newer datasets are available for topographic slope based on digital elevation models (DEMs), but we kept the FAO dataset here to allow direct comparison to LM3 as in Milly et al. (2014).

As in LM3, the bedrock conductivity is based on the recent global large-scale permeability dataset of Gleeson et al. (2011b). We interpolated this bilinearly to the land-model grid and converted to units of hydraulic conductivity, yielding a range of more than three orders of magnitude from $8.7 \times 10^{-9}\,\mathrm{m\,s^{-1}}$ to $1.6 \times 10^{-5}\,\mathrm{m\,s^{-1}}$.

Several other parameters are critical for simulating the water-table depth. The depth to bedrock z_s was set as a global constant for each simulation (Sect. 2.4). The hillslope length L was prescribed to a constant 1000 m. As in Milly et al. (2014), we used B = 200 m, noting that the hydrology is relatively insensitive to this choice given the large variability in bedrock conductivity (Gleeson et al., 2011b).

As there is a strong nonlinear interaction between soil biogeochemical cycling and water table depth, we investigated the effect of incorporating TiHy on the simulation of

HESSD
11, 8443–8492, 2014

present-day soil carbon distributions in LM3. We performed two simulations (Sect. 2.4) with the Carbon, Organisms, and Respiration in the Soil Environment (CORPSE) model, which replaces the first order, one-layer soil carbon model that is the default in LM3 (Shevliakova et al., 2009). This new model implements a comprehensive set of soil biogeochemical functions, including microbial activity and protected carbon, and will be described in detail in a forthcoming manuscript. For the sensitivity analysis performed here, there are two relevant features of CORPSE: (1) it implements vertically-resolved soil carbon states and fluxes, including aqueous leaching and a simple treatment of peat accumulation; and (2) the decomposition rate varies with soil moisture, declining to 10 % of the potential rate under saturated conditions in order to represent the effects of anoxia.

2.4 Model simulation details

Model simulations were forced by estimated historical atmospheric data (Sheffield et al., 2006). Simulations were spun up with repeated 1948–1977 forcing for 270 years and then run through a single transient period of 1948–2008. Sensitivity simulations not altering hillslope geometry shared a single 270 yr spinup, as near-surface water equilibrates relatively rapidly to changes in soil-depth scale or macroporosity, so the 1948–1988 period during the transient runs was sufficient. Analysis was conducted on the last 20 years of simulation, except when choosing specific periods to align with those of observational datasets. All simulations used a grid spacing of 2.0° latitude × 2.5° longitude. Natural vegetation and atmospheric CO_2 set to the pre-industrial concentration were used for all simulations, with no simulation of anthropogenic land use. The model configuration differed from the "LM3.1" configuration in Milly et al. (2014), in addition to these modifications and the parameters described below, also in the assumed distribution of vegetation xylem conductivity, yielding increased ET and water-table depth in the tropics, and the opposite in high latitudes (Fig. S4 in the Supplement).

HESSD
11, 8443–8492, 2014

The spinup of the deep soil water and energy states was accelerated by utilizing data from a previous spinup to initialize "dry" regions with a water table at stream height. We defined dry regions using the Budyko dryness index (Budyko, 1974) γ [–]:

$$\gamma = \frac{R_N}{H_v P}, \tag{8}$$

where R_N [W m^{-2}] is time-average net radiation, H_v [J kg^{-1}] is the heat of vaporization of water, and P [kg m^{-2} s^{-1}] is the time-average precipitation rate. On the basis of water-table tendencies from a preliminary spinup, dry regions were defined by $\gamma > 1.43$. Water tables in wet regions were initialized as follows: a mean of 10 m below the surface for the hillslope, with a horizontal water table where the water-table depth is positive and one following the surface elsewhere. Given this water-table depth, soil water content was initialized assuming a hydrostatic profile. The soil temperatures were initialized following a geothermal flux profile with the first soil layer set to the average temperature from 5 m deep in the soil from a previous spinup.

Simulations are summarized in Table 1. The Base LM3-TiHy simulation was similar to the LM3.1 configuration in Milly et al. (2014), with adjustment to soil-depth scale to improve the realism of the simulated water-table depth. It included the mean FAO slope in each gridcell with a single hillslope of linear profile shape and parallel (i.e., constant-width) plan shape. The soil-depth scale z_s was 3 m, and hydraulic conductivity associated with macroporosity K_m was 10^{-4} m s^{-1}. The Untiled simulation provided a comparison to LM3 with a configuration otherwise identical to Base. The ConstGeo simulation, with globally fixed topographic, soil, and bedrock characteristics, served as a control simulation to investigate the extent to which geographic variability in land properties explained the results attained by LM3-TiHy. The HiMacro simulation investigated the effects of higher K_m. The ShalSoil simulation was based on HiMacro and restored the shallower soil-depth scale used in Milly et al. (2014); the Concave simulation was also based on HiMacro and investigated the sensitivity to hillslope plan shape by setting $\beta = 2$ in Eq. (1). Likewise, the Converging

HESSD
11, 8443–8492, 2014

simulation was based on HiMacro and investigated the sensitivity to hillslope profile shape by setting $W = 2$ in Eq. (2). The HWSDSlope simulation was based on ShalSoil and investigated the sensitivity to topographic dataset by using the HWSD-derived topographic slope, using the mean slope for the single hillslope in each gridcell. Finally, the HWSDSlopeBimodal simulation was based on HWSDSlope but included the effects of intra-gridcell landscape-scale topographic varability by including two hillslopes per gridcell as described in Sect. 2.3.

In addition to the above simulations, we performed two simulations with CORPSE in order to investigate the sensitivity of soil carbon distribution to the inclusion of TiHy. The Untiled-CORPSE simulation was based on Untiled, and the CORPSE simulation was based on Base, except Untiled-CORPSE used $K_m = 10^{-3}\,m\,s^{-1}$ so that both models would have approximately the same geometric-mean water-table depth. This allowed us to isolate the effects of subgrid water-table heterogeneity from the effects of TiHy on the mean water-table. These simulations included an extra sequence of two runs with 1948–2008 atmospheric forcing in order to allow for additional soil carbon spinup, though additional time would have been required for full equilibrium to be reached.

2.5 Analysis and datasets for evaluation

We defined the water-table depth in two ways for analysis. A continuous function of soil state z_ψ was defined to be the lowest depth where the interpolated $\psi = 0$. However, this definition does not capture perched water tables over permafrost. Consequently, we use an alternate definition z_{wt}, the depth to the first unfrozen saturated layer, for comparisons between upland and lowland and for calculation of wetland and inundated area (below).

We diagnosed wetland area averaged over model simulation years 1993–2004, as defined by vegetated area with $z_{wt} < 0.6\,m$ for at least 1 three-month season (i.e., December-January-February, March-April-May, June-July-August, or September-October-December) in the mean annual cycle. There is no universal definition of

HESSD
11, 8443–8492, 2014

"wetland," but this definition is commensurate with those described in Mitsch and Gosselink (2007) and Fan and Miguez-Macho (2011).

Inundated area was diagnosed from the model, lacking a treatment of surface inundation and floodplain dynamics, by assuming an exponential dependence with water-table depth z_{wt} (e.g., Ringeval et al., 2010):

$$F_I = \exp\left\{-\frac{z_{wt}}{z_m}\right\}, \quad (9)$$

where the fraction F_I was evaluated separately for each tile, and $z_m = 0.3\,m$ is a parameter tuned to achieve the approximate total observed inundated area in the Base simulation. For each gridcell, we set F_I to zero for months with an average simulated ground-surface temperature below freezing. Although we emphasize that the mechanisms controlling inundation are not fully integrated into TiHy, we included this comparison because of the number of previous analyses in global wetland models comparing to or utilizing this remotely-sensed variable (Riley et al., 2011; Ringeval et al., 2012; Kleinen et al., 2012). Unlike these previous instances that used a TopModel approach, we did not make any attempt to tune local topographic parameters to match the observed inundation, and we note several potential advantages of our diagnosed inundation compared to these previous formulations. The fraction is calculated separately for each resolved tile along the hillslope, not based on the gridcell average. Moreover, the water table profile along the hillslope is explicitly calculated by the model and is not assumed to be dominated by topographic gradient as in TopModel. In addition, non-steady-state dynamics may occur, if recharge at the top of the hillslope causes a delayed increase in inundation downslope as the groundwater propagates.

We calculated spatial correlations between the observed and modelled (or diagnosed) gridcell-mean water-table depth, inundated area, and wetland area, using each land model gridcell as one data point. As we wanted to emphasize the evaluation of near-surface water-table variation important to wetlands, and not the large-magnitude variation in deep water tables in arid regions where long spinup times

HESSD
11, 8443–8492, 2014

and more detailed information about hillslope length and bedrock characteristics would be required, we used the log of the water-table depth (bounded from 0.1 to 100 m) in calculating this correlation. Likewise, to diagnose the mean bias in water-table depth for each simulation, we used the geometric mean (bounded from 0.1 m to 100 m). Because wetland is determined both in the model and in the observations as a binary variable at each location (i.e., wetland or not wetland; for each tile in the model and for location in the geographic dataset used for evaluation, below), we supplemented the correlation calculation by determining a confusion matrix (Stehman, 1997) and calculating sensitivity and precision (Altman and Bland, 1994). We used each tile as a data point, and assumed that the observed wetland fraction in each gridcell, rounded to the nearest 0.1, filled tiles from lowest to highest elevation. The sensitivity is the fraction of tiles classified in the observations as wetland that were identified as wetland in the model; the precision is the fraction of tiles identified as wetland in the model that were classified as wetland by the observations.

We evaluated the simulated water-table depth z_ψ (Sect. 3.2) by comparing it with a recent global model-data synthesis (Fan et al., 2013), which combined over 1 million site observations of water-table depth with a simple groundwater model to create a gridded dataset. The water-table depth tends to the position where the near-surface recharge (i.e., surface infiltration minus soil evaporation and transpiration) is balanced by the horizontal export of groundwater below the water table. Exporting more recharge requires a thicker portion of the bedrock and soil profile to be at full saturation (and thus at maximal hydraulic conductivity). Gleeson et al. (2011a) illustrate the range of water table regimes on a continental scale using the $\log_{10}$ of the water table ratio (WTR) Ω (Haitjema and Mitchell-Bruker, 2005):

$$\Omega = \log_{10}\left(\frac{RL}{mK_b B\zeta}\right), \tag{10}$$

where R ($\mathrm{m\,s^{-1}}$) is the recharge, and $m = 8$ for parallel (i.e., constant-width, $W = 1$) hillslope shapes. Positive values of Ω indicate that the recharge is large compared with

HESSD
11, 8443–8492, 2014

the ability of the subsurface to export this recharge horizontally and are associated with near-surface "topography-controlled" water tables, while negative values indicate comparatively low recharge and are associated with deeper "recharge-controlled" water tables. We used Ω, along with the dryness index γ, to interpret the causes of variation in the hydrological regime in different regions (Sect. 3.1). We compute Ω as in Gleeson et al. (2011a) for each gridcell using the annual-mean simulated runoff in Base (computed as precipitation minus ET, restricted to be $\geq 10^{-8}\,\mathrm{m\,yr^{-1}}$) for R, the prescribed gridcell-mean topographic slope from the FAO dataset for ζ, the prescribed bedrock hydraulic conductivity (Gleeson et al., 2011b) for K_B, and the globally constant subsurface domain depth (200 m; B) and hillslope length (1000 m; L). Although the spatial resolution of the Fan et al. (2013) dataset (0.5 min) was different than the assumed scale of hillslope tiles (100 m), we also evaluated the upland and lowland water-table depths compared to the tenth and first decile-mean (i.e., the mean between the 90th and 100th percentiles and that between the 0th and 10th percentiles) depths in the Fan et al. (2013) dataset for each land-model gridcell, respectively.

We compared diagnosed wetland area averaged over model simulation years 1993–2004 to the Global Lake and Wetland Database (GLWD) (Lehner and Doll, 2004), and we compared diagnosed inundated area to a recent multi-satellite reconstruction ranging over 1993–2004 (Papa et al., 2010) (Sect. 3.4). We used the month of maximum inundation to represent the annually inundated area for each gridcell for both the satellite reconstruction and LM3-TiHy. In each case, we interpolated the evaluation datasets to the land model resolution. For the GLWD, we first converted the Geographical Information Systems polygon raster to a regular latitude-longitude grid at 0.5 min resolution, choosing the dominant vegetation type (if present) for each 0.5 min gridcell. We then interpolated the fractions of dominant vegetation type to the land model gridcell, and summed the wetland vegetation types to yield the total wetland fraction. Some of these vegetation types consisted of wetland area-range categories (i.e., "0–25 % wetland complex"), for which we assumed the mean of the range in computing the wetland-area fraction.

HESSD
11, 8443–8492, 2014

3 Results

3.1 Typical water-table regimes

In our global LM3-TiHy simulations (Base simulation; Table 1), non-permafrost gridcells cluster in three regimes determined dually by Ω (Sect. 2.5; Fig. 4) and by the dryness index γ (Sect. 2.4): (1) a wet and poorly-drained regime where the water table is topography-controlled ($\Omega > 0$), (2) a wet and well-drained regime where the water table is recharge-controlled ($\Omega < 0$) and tends to be flat at the stream level; and (3) a dry regime where γ is large and the net recharge (after subtracting surface runoff) is negative during spinup, leading to a water table subsiding below the stream depth. In addition, a perched near-surface water table occurs over most permafrost.

A typical gridcell in the wet and poorly-drained regime is from eastern New England (Fig. 3a). Here, ample runoff ($0.588\,\mathrm{m\,yr^{-1}}$; $\gamma = 0.74$) and a low bedrock hydraulic conductivity ($8.8 \times 10^{-9}\,\mathrm{m\,s^{-1}}$; $\Omega = 1.2$) yield a near-surface water table throughout the hillslope. The water table is slightly deeper at the hilltop than near the stream, but the tendency of the water table to follow the topography while tending to zero depth at the stream elevation yields a broad portion of the landscape with a water table within the root zone. A typical gridcell in the wet and well-drained regime is from northern Florida (Fig. 3b), where there is ample runoff ($0.196\,\mathrm{m\,yr^{-1}}$; $\gamma = 1.08$) but a high bedrock conductivity typical of sandy substrates ($1.6 \times 10^{-5}\,\mathrm{m\,s^{-1}}$; $\Omega = -2.2$). Throughout the hillslope, the water table tends towards the stream elevation, with only a slight increase in water table height towards the hilltop required to maintain a sufficient hydraulic gradient to export the recharge towards the stream. Only the lowland tile has a water table within the root zone. Finally, a gridcell typical of the dry regime is in the Colorado Rocky mountains (Fig. 3c). The annual-mean difference between precipitation and evaporation is entirely balanced by surface runoff ($\gamma = 2.46$), so the water table subsides below the stream elevation as a result of lowland ET. This subsidence is relatively slow during model spin-up due to the low bedrock conductivity ($10^{-8}\,\mathrm{m\,s^{-1}}$; $\Omega = 0.6$); other regions with large γ but higher bedrock conductivity require

HESSD
11, 8443–8492, 2014

a shorter spin-up period for substantial subsidence. Additional diagnostics of hillslope behaviour are illustrated in Figs. S1–2 in the Supplement.

The three regimes of water table behaviour are readily illustrated globally (Fig. 4). The diagnostics Ω (Fig. 4a; computed based on variables shown in Fig. 4b–d) and γ (Fig. 4e) determine which of the three regimes each gridcell is characteristic of, and largely determine the simulated water-table depth (Sect. 3.2). Areas with $\gamma > \sim 1.43$, such as the Western US, North and South Africa, and Australia, define the range of the dry regime. Areas with a topography-controlled water table (determined largely by having low bedrock conductivity and low γ), such as New England and Eastern Scandinavia/Baltic states, comprise the wet, poorly-drained regime. Finally, areas with a recharge-controlled water table (determined largely by having high bedrock conductivity and low γ), such as the Southeastern US and Central Europe, comprise the wet, well-drained regime.

3.2 Evaluation of water-table depth

We compared the gridcell-mean water-table depth z_ψ simulated in LM3-TiHy (Base simulation) to the Fan et al. (2013) model-data synthesis (Fig. 5a and b). As Fan et al. (2013) only partially consider perched water tables in permafrost areas, we excluded permafrost gridcells from this comparison. The general pattern of water-table depth in LM3-TiHy (Fig. 5a) is explained by Fig. 4: wet areas with topography-controlled water tables have areal-mean water-table depths less than 10 m. These include the Northeastern US, Scandinavia and the Baltic states, Central Africa, parts of the Amazon, and Southeast Asia. In some of these areas, such as in the Northeastern US and Scandinavia, the water table is biased high compared with the model-data synthesis (Fig. 5b). This may be partly due to the lack of representation in LM3-TiHy of anthropogenic drainage of wetlands and groundwater pumping in populated areas. In drier areas without net recharge to sustain a high water table, LM3-TiHy and the model-data synthesis tend to agree that the water table is deeper than 20–30 m. The greater depth in some dry regions in the model-data synthesis may be due to the limited spinup

HESSD
11, 8443–8492, 2014

of these regions in LM3-TiHy. LM3-TiHy also fails to resolve the widespread wetlands (water-table depth < 1 m) in the Hudson Bay Lowlands and the Ob Valley that appear in the model-data synthesis; this is likely due to the lack of floodplain and peatland processes in LM3-TiHy. Over all non-permafrost soil area, the correlation between the two representations is 0.31, with a geometric mean of 15 m in LM3-TiHy slightly shallower than the geometric mean of 18 m in the model-data synthesis. This low bias in global-mean water-table depth is expected due to the finite spinup in the dry regime. When comparing the areal frequency distributions of water-table depth independent of geographic location (Fig. 5d), LM3-TiHy matches the distribution in the model-data synthesis well. There is slight under-prediction of near-zero water-table depth area, possibly due to the lack of inundation processes in the model. A moderate under-prediction of very large water-table depths is consistent with the low mean water-table-depth bias.

We investigated the extent to which water-table depths simulated by LM3-TiHy were determined by land properties as opposed to atmospheric forcing climate. The water-table depth in the ConstGeo simulation (Fig. 5c) is degraded compared to the Base simulation (with a correlation reduced to 0.15): the ConstGeo simulation under-predicts both very shallow water tables in low-slope, poorly drained regions that are also wet (e.g., the western Amazon, Quebec, and the Baltic states), and very deep water tables in high-slope, well-drained regions that are also dry (e.g., the non-coastal western US).

Unlike previous land models suitable for coupling into an ESM, LM3-TiHy is capable of simulating distinct water-table depths in the upland and lowland portions of each gridcell (here using the z_{wt} definition of water-table depth from Sect. 2.5 to include the permafrost area). In the upland (Fig. 6a), only permafrost regions have water-table depths < 1 m, and only a few very wet and/or poorly drained areas outside permafrost (e.g., the Western Amazon, the Baltic states, and parts of Indonesia) have water-table depths < 10 m. In the dry and/or well-drained areas comprising the bulk of the temperate and tropical land area, the upland water table is deeper than 30 m. These depths are consistent with the model-data synthesis tenth-decile water-table depth

HESSD
11, 8443–8492, 2014

(Fig. 6b), except for the insufficiently shallow water tables in the Hudson Bay Lowland and Ob Valley peatlands noted in the gridcell-mean comparison above. In contrast, most of the wet areas of the world with non-negligible recharge, in addition to most of the permafrost, have a lowland water-table depth < 1 m (Fig. 6c). This is also true for the first decile in the model-data synthesis (Fig. 6d), although over somewhat more widespread areas in the synthesis, particularly in subtropical Africa, Asia, and Australia. The difference in water-table depth between the upland and lowland simulated in each LM3-TiHy gridcell leads to simulated differences in both surface energy fluxes and in vegetation properties, to be discussed next.

3.3 Simulated differences in surface fluxes and properties between lowlands and uplands

A wide range of areas have much shallower water tables in the lowland portion of the gridcell than the upland (Fig. 6a and c). The shallower water tables in lowland areas with moderately wet and well- to moderately-well-drained soils enhance water availability for transpiration and ground evaporation, causing an increase in ET in many regions of 100–1000 mm yr^{-1} as compared with the uplands in the same gridcells (Fig. 7b). These regions tend to be marginally-wet and subtropical areas where potential ET exceeds available precipitation in some seasons, but the annual precipitation is still large enough to support groundwater convergence to the lowlands. Compared with uplands, the larger ET in the lowlands is associated with a lower Bowen ratio and thus a ground-surface temperature lower by 1–4 K (Fig. 7d). Some northern-latitude lowlands have slightly higher (< 0.5 K) annual-mean temperatures compared with uplands due to the effects of increased soil moisture on soil thermal properties in soils undergoing seasonal freeze–thaw (Subin et al., 2013). The groundwater convergence and higher ET in lowlands causes vegetation greening, with values of leaf area index (LAI) 1–5 higher compared with uplands in the same gridcells (Fig. 7f).

HESSD
11, 8443–8492, 2014

3.4 Evaluation of diagnosed wetland area and inundated area

We compared the wetland fraction diagnosed from the model (as defined in Sect. 2.5) to the GLWD (Fig. 8a and b). The Base simulation diagnoses major wetland areas in the same regions as GLWD: Northern Canada, Alaska, Brazil, Russia, South Asia, Central Africa, and Indonesia. However, total simulated wetland area (14.4 million km^2) is larger than the interpolated GLWD area of 6.2 million km^2 and includes both more regions with high fraction and larger areas of diffuse wetland. However, some of the diffuse wetland area in GLWD was lost as an artefact of our interpolation procedure, contributing to this apparent bias: Lehner and Doll (2004) suggest 8.2–10.1 million km^2 of total wetland was contained in their dataset. The spatial correlation is 0.32, with a higher sensitivity (47 %) than precision (20 %) consistent with the high bias in the model. Similar to the comparison of simulated water-table depth, the Hudson Bay Lowlands are not well-represented by the model, with major wetland area occurring farther to the north than observed. This may be due to the failure to capture the low slope of this region in our implementation of the FAO dataset (Sects. 2.3 and 3.7). The wetland diagnosed in the Ob Valley is also not as prominent as observed, and there are wider areas of wetlands in the Eastern Siberian permafrost, the Amazon, and Indonesia than observed. We note the uncertainty in existing wetland datasets: the Matthews and Fung (1987) dataset only has a correlation of 0.54 with the GLWD.

The inundated area based on the multi-satellite reconstruction (Fig. 8c) (Papa et al., 2010) overlaps substantially with the GLWD wetland area, with some important differences: more diffuse area, farther north concentrations in Canada (including areas in the Newfoundland and the Canadian Shield more prominently than the Hudson Bay Lowlands), and the addition of apparent irrigated cropland and/or floodplains in the Mississippi Valley, India, Southeast Asia, and eastern China. The Base inundation fraction (Fig. 8d) comparison is less favourable (correlation 0.18) than that for wetland area, due to additional large areas of simulated inundation in permafrost zones not found in observations, along with missing inundated areas in the Mississippi Valley and

HESSD
11, 8443–8492, 2014

South and Eastern Asia, which may be due to the lack of representation of irrigated cropland in the model. The extent of maximum annual inundated area simulated by the model (10.6 million km^2) compares more favourably to that in the satellite reconstruction of 10.1 million km^2, but this is largely due to the tuning of z_m to 0.3 m. The fine-scale spatial mismatches in inundated area account for temporal mismatches, both seasonally and inter-annually, when we compared against the full monthly 1993–2004 satellite reconstruction timeseries (not shown). However, a comparison of the areal frequency distribution of inundated area shows good model performance (Fig. 8e), with a slight modelled unrealistic peak just below 0.1 likely due to the discretization of the hillslopes into 10 tiles.

3.5 Comparison to the untiled LM3

We compared the Base simulation to the Untiled simulation, which uses LM3 identically configured as Base except without using TiHy. The water-table depth (Fig. 5e) in Untiled has a substantial shallow bias of 8 m. As the untiled LM3 has only a gridcell-mean water-table depth, the diagnosis of wetland area was degraded compared with Base (Table 2); most of the wetland area corresponds with high water tables in permafrost and the central Amazon (not shown). The diagnosis of the continuously defined inundated area in Untiled was biased low but not with degraded correlation. Even though there is more ET in lowlands than uplands in Base (Fig. 7d), the exchanges of water and energy with the atmosphere are little changed in the gridcell-mean between Base and Untiled (Figs. 7a, c and 9a–d). The global mean LAI is also minimally changed on average in Base as compared with Untiled (Fig. 9f; increase of 0.04 averaged over all soil area), but there are regions with changes of ±1–2. These changes result from the compensation between two factors: the large LAI in lowlands in Base (Fig. 7f), and the 7 m deeper mean water table in Base compared with Untiled (Fig. 5a and e). The proportionally larger increase in LAI in lowlands as compared with the increase in ET (relative to the uplands in Base) illustrates the nonlinear coupling between hydrology and biogeochemistry.

HESSD
11, 8443–8492, 2014

3.6 Sensitivity of soil carbon distribution to subgrid water-table heterogeneity

We compared the soil carbon distributions simulated in CORPSE-Untiled and CORPSE (Fig. 10a and b). Although changes in physical fluxes were very small and changes in LAI were small between Untiled and Base (Sect. 3.5), the partially-spun-up CORPSE simulated a global soil carbon total of 951 Pg C, compared with only 603 Pg C in the comparatively-spun-up CORPSE-Untiled. This occurred despite the simulations sharing a geometric mean water-table depth of 15 m (Table 2). This large difference illustrates the strong nonlinear coupling between soil carbon cycling and hydrology. Although both simulations predicted large soil carbon accumulations ($\sim 50\,\mathrm{kg\,C\,m^{-2}}$) in permafrost, only CORPSE with TiHy additionally simulated substantial accumulations (~ 5–$10\,\mathrm{kg\,C\,m^{-2}}$) in areas of the world with some wetland fraction (Fig. 8b), such as Northern Europe, the Amazon, and Southeast Asia. While upland soil carbon accumulations in CORPSE (Fig. 10c) were similar to the gridcell-mean values in CORPSE-Untiled, lowlands accumulated more than four times as much carbon per unit area, explaining the greater global total.

3.7 Sensitivity to alternative parameter choices and datasets

We investigated the sensitivity of simulated hydrology to macropore conductivity (K_m), the depth of conductive soil (z_s), the hillslope shape, and the slope (ζ). In general, increasing the effect of macroporosity, increasing the depth of conductive soil, making the hillslope shape less concave, and increasing the topographic slope all act to lower the water table by facilitating the export of recharge downslope. The sensitivity experiments show mixed effects on the evaluation of simulated water-table depth, wetland extent, and inundated area extent (Table 2), with no one configuration proving superior for all metrics. In the HiMacro simulation, increasing K_m from 0.1 to $1.0\,\mathrm{mm\,s^{-1}}$ increases the proportion of within-soil horizontal water flow relative to surface runoff (not shown), raising the water-table correlation but lowering the mean water table and drastically reducing the simulated wetland and inundated area, degrading the

HESSD
11, 8443–8492, 2014

comparison to observed wetland and inundated area. Using $K_m = 1.0\,mm\,s^{-1}$ but reducing the soil-depth scale from 3 to 1 m (ShalSoil) compensates by raising the water table, improving the comparison to observed wetland and inundated area, though the correlation with water-table depth was degraded. Using concave hillslope shape (but with the original 3 m soil-depth scale; Concave) raises the average water table and increases the wetland and inundated area, making it more diffuse (i.e., larger regions with low area fraction). This improves the simulations, except for a low bias in inundated area. Converging hillslopes (Converging) slightly increase the water table in lowlands (not shown) as compared with HiMacro, but the relatively smaller area of lowlands causes a net decrease in simulated wetland and inundated area. Using the HWSD topographic slope dataset instead of the original FAO dataset (HWSDSlope) improves the correlation of all three variables evaluated but leads to under-prediction of inundated and wetland area. Including two hillslopes in each gridcell to represent separately the low-slope and high-slope area fractions (HWSDSlopeBimodal) raises the average water table and the wetland and inundated area, though lowering the correlation of wetland area with observed. In HWSDSlopeBimodal, the low water table bias in the Hudson Bay Lowlands in Base is reduced (Fig. S3f in the Supplement), as the HWSD slope dataset more appropriately represents the very low topographic slope of this region ($\sim$ 0.01–0.02). Finally, the ConstGeo simulation shows that degraded simulation of the water-table depth (Sect. 3.2) has little effect on the quality of simulated wetland and inundated area, as the correlations for these metrics are within the range of the other sensitivity experiments. Water-table depths for these sensitivity experiments are illustrated in Fig. S3 in the Supplement.

4 Discussion and conclusions

We incorporated into a land model (capable of being coupled into an ESM) a dynamic representation of wetland area, with distinct vegetation properties resolved in wetlands, using a novel approach based on the inclusion of representative hillslope patches

HESSD
11, 8443–8492, 2014

or “tiles”. Including this representation allowed the simulation of a gradient in water-table depths from lowland to upland in each land model gridcell. The shallower water table in lowlands due to lower elevation and groundwater convergence from uplands allowed increased ET and increased vegetation LAI in many regions as compared with uplands. The increased LAI in lowlands is commonly observed, so comparison with field transects and remotely-sensed observations would allow us to quantify the accuracy of the LM3-TiHy prediction. In some areas, the LAI increases predicted in lowlands as compared with uplands in LM3-TiHy may be excessive, as the upper limit of LAI in LM3 (i.e., reaching 10 in the Boreal forest) is excessive.

Gridcell-mean surface energy and water fluxes were little changed by the inclusion of subgrid heterogeneity in water-table depth, but substantial changes in biogeochemistry occurred. The mean LAI was minimally changed even though the mean water-table depth was larger with the inclusion of subgrid heterogeneity, potentially illustrating the nonlinear coupling between hydrology and biogeochemistry. This nonlinearity was more strongly apparent in its effects on simulated soil carbon distributions. Although we used an intermediate version of a developing soil-carbon model (CORPSE) with a partial spinup and did not compare to observed soil carbon distributions, the large increase in global soil carbon simulated in LM3-TiHy illustrated the importance of considering subgrid wetlands in modelling present-day soil carbon distributions.

As none of the CMIP5 models included belowground heterogeneity in natural ecosystems (Todd-Brown et al., 2014), current estimates of future changes in soil carbon may be biased low due to their incapability of simulating existing wetland carbon that is vulnerable to future environmental change. In addition to subgrid horizontal heterogeneity, vertically-resolved soil carbon states and fluxes may be necessary to appropriately model the decline in soil decomposition below the water table. The importance of modelling vertical heterogeneity in soil carbon has also been illustrated for permafrost processes (Koven et al., 2013, 2011), but the CMIP5 models all lacked this feature as well.

HESSD
11, 8443–8492, 2014

The simulated water-table depth depended primarily on the net simulated recharge (largely a function of the dryness index indicating the availability of water in excess of ET for runoff), the slope, and the bedrock permeability. A control simulation omitting geographic variability in land characteristics simulated a degraded water-table depth distribution, showing that both climate and land characteristics are necessary for realistic simulations of water-table depth. Alternative representations of the slope, hillslope shape, and the soil hydraulic conductivity had large effects on the location of the water table when it was near the surface, and thus on the simulated wetland and inundated area, indicating the need for better datasets to prescribe or parameterize these variables globally. Our simulations included global constants for soil-depth scale and hillslope length (i.e., one-half the distance between streams), and future simulations may be improved by incorporating geographic variation in these parameters as data become available. As only one global dataset of bedrock permeability exists (Gleeson et al., 2011b), sensitivity to these data should be investigated when alternatives become available, as the wide range in bedrock hydraulic conductivity among regions was a strong control on the water table regime.

The model captured some of the spatial variability in water-table depth and diagnosed wetland area, with substantial room for improved parameterization. Better observations of inundated area are available than of wetland ecosystem extent, and inundated area proved more difficult to diagnose from the model, which was not geographically parameterized to match observed inundated area. This is likely due to the lack of representation of microtopography, non-instantaneous surface runoff, and floodplain dynamics that create inundation in some regions (Fan and Miguez-Macho, 2011). LM3-TiHy, like most other published global wetland representations, can only indirectly diagnose inundation as some function of area with a near-surface water table: however, a near-surface water table is a prerequisite to inundation rather than a sufficient condition. We do note that wetlands fed by groundwater discharge or impeded drainage, which should be able to be simulated by TiHy with sufficient-quality input data, are more temporally stable than other types of wetlands such as those

HESSD
11, 8443–8492, 2014

resulting from river flooding (Fan and Miguez-Macho, 2011), and thus more likely to be associated with biogeochemical differences from uplands.

We found that in LM3-TiHy, degrading the representation of land properties and thus the water-table depth had little effect on the simulated wetland and inundated areas. In addition, using an improved topographic slope dataset improved the simulated water-table depth but not the wetland and inundated areas. From this we can conclude that either forcing climate alone is largely sufficient to predict these hydrological variables, or that LM3-TiHy with its current input datasets is missing some of the key controls of these hydrological variables (or some combination of these two conclusions). However, the inclusion of subgrid heterogeneity in water-table depth based on a representative hillslope shape did improve the simulation of wetland and inundated areas, regardless of geographic variation in land properties.

Additional future work could include a larger hillslope length in arid regions to allow the simulation of arid oases (Fan and Miguez-Macho, 2011). In addition, inclusion of anthropogenic processes such as groundwater pumping, irrigation in croplands, and intentional drainage of natural wetlands could improve the model's representation of present-day wetlands, which have been altered from their natural extent. Inclusion of regional-scale groundwater flow (i.e., between hillslopes or between gridcells), might improve simulations in some regions. Finally, in this study, we focused on inter-gridcell variation in land properties (except for a simple inclusion of subgrid variation in topographic slope in HWSDBimodal). However, intra-hillslope variation in subsurface properties, such as greater soil thickness in lowlands (e.g., Fan and Miguez-Macho, 2011), may also be important to wetland dynamics.

Further evaluation of the hillslope hydrology at sites or regions where the topography, substrate properties, forcing climate, and resulting hydrology are well characterized could allow improved confidence in the fidelity of the model. Along with improvements in the representation of physical hydrological processes within the model, the inclusion of additional biogeochemical processes would be required to allow the representation of peatlands, such as bryophyte vegetation and dynamic soil properties.

HESSD
11, 8443–8492, 2014

Nevertheless, while additional model development challenges remain, LM3-TiHy represents the implementation of a new approach towards the mechanistic representation of wetlands and other features of fine-scale hydrological heterogeneity in an ESM. Such a representation is necessary for accurately predicting the responses of peatland soil carbon, natural methane emissions, and wetland area distributions under future climate change.

The Supplement related to this article is available online at doi:10.5194/hessd-11-8443-2014-supplement.

Acknowledgements. The authors thank Steve Pacala (Princeton University) for ideas during the initial model development. Nir Krakauer (City University of New York) and Ying Fan (Rutgers University) contributed suggestions for a draft version of this manuscript. Sebastien Biraud (Lawrence Berkeley National Laboratory), Joe Melton (Environment Canada), and Jasmin John (GFDL) provided assistance with interpolated observational datasets. This research was supported by the US Department of Agriculture under project #2011–67003-30373 and the National Aeronautics and Space Administration through the Jet Propulsion Laboratory, subcontract 1430081. Facilities and computational resources were provided by the US Geophysical Fluid Dynamics Laboratory, administered by the National Oceanic and Atmospheric Administration.

References

Altman, D. G. and Bland, J. M.: Statistics notes – diagnostic-tests-1 – sensitivity and specificity, Brit. Med. J., 308, 1552–1552, 1994.

Atchley, A. L. and Maxwell, R. M.: Influences of subsurface heterogeneity and vegetation cover on soil moisture, surface temperature and evapotranspiration at hillslope scales, Hydrogeol. J., 19, 289–305, doi:10.1007/s10040-010-0690-1, 2011.

HESSD
11, 8443–8492, 2014

Beven, K. J. and Kirkby, M. J.: A physically based, variable contributing area model of basin hydrology/Un modèle à base physique de zone d'appel variable de l'hydrologie du bassin versant, Hydrol. Sci. Bull., 24, 43–69, doi:10.1080/02626667909491834, 1979.

Bohn, T. J. and Lettenmaier, D. P.: Systematic biases in large-scale estimates of wetland methane emissions arising from water table formulations, Geophys. Res. Lett., 37, 6, L22401, doi:10.1029/2010gl045450, 2010.

Bohn, T. J., Podest, E., Schroeder, R., Pinto, N., McDonald, K. C., Glagolev, M., Filippov, I., Maksyutov, S., Heimann, M., Chen, X., and Lettenmaier, D. P.: Modeling the large-scale effects of surface moisture heterogeneity on wetland carbon fluxes in the West Siberian Lowland, Biogeosciences, 10, 6559–6576, doi:10.5194/bg-10-6559-2013, 2013.

Bonan, G., Levis, S., Kergoat, L., and Oleson, K.: Landscapes as patches of plant functional types: an integrating concept for climate and ecosystem models, Global Biogeochem. Cy., 16, 5-1–5-23, doi:10.1029/2000GB001360, 2002.

Budyko, M. I.: Climate and life, International Geophysical Series, 18, Academic Press, New York, 1974.

Buffam, I., Turner, M. G., Desai, A. R., Hanson, P. C., Rusak, J. A., Lottig, N. R., Stanley, E. H., and Carpenter, S. R.: Integrating aquatic and terrestrial components to construct a complete carbon budget for a north temperate lake district, Glob. Change Biol., 17, 1193–1211, doi:10.1111/j.1365-2486.2010.02313.x, 2011.

Campoy, A., Ducharne, A., Cheruy, F., Hourdin, F., Polcher, J., and Dupont, J. C.: Response of land surface fluxes and precipitation to different soil bottom hydrological conditions in a general circulation model, J. Geophys. Res.-Atmos., 118, 10725–10739, doi:10.1002/jgrd.50627, 2013.

Choi, H. I. and Liang, X. Z.: Improved terrestrial hydrologic representation in mesoscale land surface models, J. Hydrometeorol., 11, 797–809, doi:10.1175/2010jhm1221.1, 2010.

Choi, H. I., Kumar, P., and Liang, X. Z.: Three-dimensional volume-averaged soil moisture transport model with a scalable parameterization of subgrid topographic variability, Water Resour. Res., 43, W04414, doi:10.1029/2006wr005134, 2007.

Ciais, P., Sabine, C., Bala, G., Bopp, L., Brovkin, V., Canadell, J., Chhabra, A., DeFries, R., Galloway, J., Heimann, M., Jones, C., C., L. Q., Myneni, R. B., Piao, S., and Thornton, P.: Carbon and other biogeochemical cycles, in: Climate Change 2013: The Physical Science Basis. Contribution of Working Group I to the Fifth Assessment Report of the Intergovernmental Panel on Climate Change, edited by: Stocker, T. F., Qin, D., Plattner, G.-

HESSD
11, 8443–8492, 2014

K., Tignor, M., Allen, S. K., Boschung, J., Nauels, A., Xia, Y., Bex, V., and Midgley, P. M., Cambridge University Press, New York, NY, 2013.
Fan, Y. and Miguez-Macho, G.: A simple hydrologic framework for simulating wetlands in climate and earth system models, Clim. Dynam., 37, 253–278, doi:10.1007/s00382-010-0829-8, 2011.
Fan, Y., Li, H., and Miguez-Macho, G.: Global patterns of groundwater table depth, Science, 339, 940–943, doi:10.1126/science.1229881, 2013.
FAO/IIASA/ISRIC/ISSCAS/JRC: Harmonized World Soil Database, Rome, Italy, available at: http://webarchive.iiasa.ac.at/Research/LUC/External-World-soil-database/HTML/HWSD_Data.html?sb=4, (last access: 16 May 2013), 2012.
FAO/UNESCO: Digital Soil Map of the World and Derived Soil Properties, CD-ROM, Version 3.6, Rome, Food and Agricultural Organization, 2003.
Frolking, S., Roulet, N., and Lawrence, D.: Issues related to incorporating northern peatlands into global climate models, in: Carbon Cycling in Northern Peatlands, AGU Monograph, 184, 19–35, doi:10.1029/2008gm000809, 2009.
Frolking, S., Talbot, J., Jones, M. C., Treat, C. C., Kauffman, J. B., Tuittila, E. S., and Roulet, N.: Peatlands in the Earth's 21st century climate system, Environ. Rev., 19, 371–396, doi:10.1139/a11-014, 2011.
Gerber, S., Hedin, L. O., Keel, S. G., Pacala, S. W., and Shevliakova, E.: Land use change and nitrogen feedbacks constrain the trajectory of the land carbon sink, Geophys. Res. Lett., 40, 5218–5222, doi:10.1002/grl.50957, 2013.
Gleeson, T., Marklund, L., Smith, L., and Manning, A. H.: Classifying the water table at regional to continental scales, Geophys. Res. Lett., 38, L05401, doi:10.1029/2010GL046427, 2011a.
Gleeson, T., Smith, L., Moosdorf, N., Hartmann, J., Durr, H. H., Manning, A. H., van Beek, L. P. H., and Jellinek, A. M.: Mapping permeability over the surface of the Earth, Geophys. Res. Lett., 38, L02401, doi:10.1029/2010GL045565, 2011b.
Grosse, G., Harden, J., Turetsky, M., McGuire, A. D., Camill, P., Tarnocai, C., Frolking, S., Schuur, E. A. G., Jorgenson, T., Marchenko, S., Romanovsky, V., Wickland, K. P., French, N., Waldrop, M., Bourgeau-Chavez, L., and Striegl, R. G.: Vulnerability of high-latitude soil organic carbon in North America to disturbance, J. Geophys. Res., 116, G00K06, doi:10.1029/2010JG001507, 2011.
Gulden, L. E., Rosero, E., Yang, Z. L., Rodell, M., Jackson, C. S., Niu, G. Y., Yeh, P. J. F., and Famiglietti, J.: Improving land-surface model hydrology: is an explicit aquifer model better

HESSD
11, 8443–8492, 2014

than a deeper soil profile?, Geophys. Res. Lett., 34, L09402, doi:10.1029/2007GL029804, 2007.
Haitjema, H. M. and Mitchell-Bruker, S.: Are water tables a subdued replica of the topography?, Ground Water, 43, 781–786, doi:10.1111/j.1745-6584.2005.00090.x, 2005.
Hilberts, A. G. J., Troch, P. A., Paniconi, C., and Boll, J.: Low-dimensional modeling of hillslope subsurface flow: Relationship between rainfall, recharge, and unsaturated storage dynamics, Water Resour. Res., 43, W03445, doi:10.1029/2006WR004964, 2007.
Jackson, R. B., Canadell, J., Ehleringer, J. R., Mooney, H. A., Sala, O. E., and Schulze, E. D.: A global analysis of root distributions for terrestrial biomes, Oecologia, 108, 389–411, doi:10.1007/bf00333714, 1996.
Jackson, R. B., Mooney, H. A., and Schulze, E. D.: A global budget for fine root biomass, surface area, and nutrient contents, P. Natl. Acad. Sci. USA, 94, 7362–7366, doi:10.1073/pnas.94.14.7362, 1997.
Kassas, M.: Habitat and plant communities in the Egyptian desert: I. Introduction, J. Ecol., 40, 342–351, doi:10.2307/2256804, 1952.
Kleinen, T., Brovkin, V., and Schuldt, R. J.: A dynamic model of wetland extent and peat accumulation: results for the Holocene, Biogeosciences, 9, 235–248, doi:10.5194/bg-9-235-2012, 2012.
Koirala, S., Yeh, P. J. F., Hirabayashi, Y., Kanae, S., and Oki, T.: Global-scale land surface hydrologic modeling with the representation of water table dynamics, J. Geophys. Res.-Atmos., 119, 75–89, doi:10.1002/2013JD020398, 2013.
Koven, C. D., Ringeval, B., Friedlingstein, P., Ciais, P., Cadule, P., Khvorostyanov, D., Krinner, G., and Tarnocai, C.: Permafrost carbon-climate feedbacks accelerate global warming, P. Natl. Acad. Sci. USA, 108, 14769–14774, doi:10.1073/pnas.1103910108, 2011.
Koven, C. D., Riley, W. J., Subin, Z. M., Tang, J. Y., Torn, M. S., Collins, W. D., Bonan, G. B., Lawrence, D. M., and Swenson, S. C.: The effect of vertically resolved soil biogeochemistry and alternate soil C and N models on C dynamics of CLM4, Biogeosciences, 10, 7109–7131, doi:10.5194/bg-10-7109-2013, 2013.
Krakauer, N. Y., Puma, M. J., and Cook, B. I.: Impacts of soil–aquifer heat and water fluxes on simulated global climate, Hydrol. Earth Syst. Sci., 17, 1963–1974, doi:10.5194/hess-17-1963-2013, 2013.
Krakauer, N. Y., Li, H., and Fan, Y.: Groundwater flow across spatial scales: importance for climate modeling, Environ. Res. Lett., 9, 034003, doi:10.1088/1748-9326/9/3/034003, 2014.

HESSD
11, 8443–8492, 2014

Lawrence, D. M., Oleson, K. W., Flanner, M. G., Thornton, P. E., Swenson, S. C., Lawrence, P. J., Zeng, X., Yang, Z.-L., Levis, S., Sakaguchi, K., Bonan, G. B., and Slater, A. G.: Parameterization improvements and functional and structural advances in version 4 of the Community Land Model, J. Adv. Mod. Earth Sys., 3, 5218–5222, doi:10.1029/2011MS000045, 2011.

Lehner, B. and Doll, P.: Development and validation of a global database of lakes, reservoirs and wetlands, J. Hydrol., 296, 1–22, doi:10.1016/j.jhydrol.2004.03.028, 2004.

Leung, L. R., Huang, M. Y., Qian, Y., and Liang, X.: Climate-soil-vegetation control on groundwater table dynamics and its feedbacks in a climate model, Clim. Dynam., 36, 57–81, doi:10.1007/s00382-010-0746-x, 2011.

Limpens, J., Berendse, F., Blodau, C., Canadell, J. G., Freeman, C., Holden, J., Roulet, N., Rydin, H., and Schaepman-Strub, G.: Peatlands and the carbon cycle: from local processes to global implications – a synthesis, Biogeosciences, 5, 1475–1491, doi:10.5194/bg-5-1475-2008, 2008.

Lo, M. H. and Famiglietti, J. S.: Precipitation response to land subsurface hydrologic processes in atmospheric general circulation model simulations, J. Geophys. Res., 116, D05107, doi:10.1029/2010JD015134, 2011.

Matthews, E. and Fung, I.: Methane emission from natural wetlands: global distribution, area, and environmental characteristics of sources, Global Biogeochem. Cy., 1, 61–86, doi:10.1029/GB001i001p00061, 1987.

Maxwell, R. M., Lundquist, J. K., Mirocha, J. D., Smith, S. G., Woodward, C. S., and Tompson, A. F. B.: Development of a coupled groundwater-atmosphere model, Mon. Weather Rev., 139, 96–116, doi:10.1175/2010mwr3392.1, 2011.

Merot, P., Squividant, H., Aurousseau, P., Hefting, M., Burt, T., Maitre, V., Kruk, M., Butturini, A., Thenail, C., and Viaud, V.: Testing a climato-topographic index for predicting wetlands distribution along an European climate gradient, Ecol. Model., 163, 51–71, doi:10.1016/s0304-3800(02)00387-3, 2003.

Miguez-Macho, G., Fan, Y., Weaver, C. P., Walko, R., and Robock, A.: Incorporating water table dynamics in climate modeling: 2. Formulation, validation, and soil moisture simulation, J. Geophys. Res., 112, D13108, doi:10.1029/2006JD008112, 2007.

Milly, P. C., Malyshev, S. L., Shevliakova, E., Dunne, K. A., Findell, K. L., Gleeson, T., Liang, Z., Phillips, P., Stouffer, R. J., and Swenson, S.: An enhanced model of land water and energy

HESSD
11, 8443–8492, 2014

for global hydrologic and earth-system studies, J. Hydrometeorol., doi:10.1175/JHM-D-13-0162.1, online first, 2014.
Milly, P. C. D. and Shmakin, A. B.: Global modeling of land water and energy balances, Part I: the land dynamics (LaD) model, J. Hydrometeorol., 3, 283–299, doi:10.1175/1525-7541(2002)003<0283:gmolwa>2.0.co;2, 2002.
Mitsch, W. J. and Gosselink, J. G.: Wetlands, 4th Edn., John Wiley & Sons, New York, 582 pp., 2007.
Niu, G. Y., Yang, Z. L., Dickinson, R. E., Gulden, L. E., and Su, H.: Development of a simple groundwater model for use in climate models and evaluation with Gravity Recovery and Climate Experiment data, J. Geophys. Res., 112, D07103, doi:10.1029/2006JD007522, 2007.
Nykanen, D. K. and Foufoula-Georgiou, E.: Soil moisture variability and scale-dependency of nonlinear parameterizations in coupled land–atmosphere models, Adv. Water Resour., 24, 1143–1157, doi:10.1016/s0309-1708(01)00046-x, 2001.
O'Grady, A. P., Carter, J. L., and Bruce, J.: Can we predict groundwater discharge from terrestrial ecosystems using existing eco-hydrological concepts?, Hydrol. Earth Syst. Sci., 15, 3731–3739, doi:10.5194/hess-15-3731-2011, 2011.
Pan, L., Jin, J., Miller, N., Wu, Y.-S., and Bodvarsson, G.: Modeling hydraulic responses to meteorological forcing: from canopy to aquifer, Vadose Zone J., 7, 325–331, 2008.
Paniconi, C., Troch, P. A., van Loon, E. E., and Hilberts, A. G. J.: Hillslope-storage Boussinesq model for subsurface flow and variable source areas along complex hillslopes: 2. Intercomparison with a three-dimensional Richards equation model, Water Resour. Res., 39, 1317, doi:10.1029/2002WR001730, 2003.
Papa, F., Prigent, C., Aires, F., Jimenez, C., Rossow, W. B., and Matthews, E.: Interannual variability of surface water extent at the global scale, 1993–2004, J. Geophys. Res., 115, D12111, doi:10.1029/2009jd012674, 2010.
Rihani, J. F., Maxwell, R. M., and Chow, F. K.: Coupling groundwater and land surface processes: idealized simulations to identify effects of terrain and subsurface heterogeneity on land surface energy fluxes, Water Resour. Res., 46, W12523, doi:10.1029/2010WR009111, 2010.
Riley, W. J., Subin, Z. M., Lawrence, D. M., Swenson, S. C., Torn, M. S., Meng, L., Mahowald, N. M., and Hess, P.: Barriers to predicting changes in global terrestrial methane

HESSD
11, 8443–8492, 2014

fluxes: analyses using CLM4Me, a methane biogeochemistry model integrated in CESM, Biogeosciences, 8, 1925–1953, doi:10.5194/bg-8-1925-2011, 2011.
Ringeval, B., Noblet-Ducoudre, N. D., Ciais, P., Bousquet, P., Prigent, C., Papa, F., Rossow, W. B., and de Noblet-Ducoudre, N.: An attempt to quantify the impact of changes in wetland extent on methane emissions on the seasonal and interannual time scales, Global Biogeochem. Cy., 24, GB2003, doi:10.1029/2008GB003354, 2010.
Ringeval, B., Decharme, B., Piao, S. L., Ciais, P., Papa, F., de Noblet-Ducoudré, N., Prigent, C., Friedlingstein, P., Gouttevin, I., Koven, C., and Ducharne, A.: Modelling sub-grid wetland in the ORCHIDEE global land surface model: evaluation against river discharges and remotely sensed data, Geosci. Model Dev., 5, 941–962, doi:10.5194/gmd-5-941-2012, 2012.
Schuldt, R. J., Brovkin, V., Kleinen, T., and Winderlich, J.: Modelling Holocene carbon accumulation and methane emissions of boreal wetlands – an Earth system model approach, Biogeosciences, 10, 1659–1674, doi:10.5194/bg-10-1659-2013, 2013.
Schuur, E., Bockheim, J., Canadell, J., Euskirchen, E., Field, C., Goryachkin, S., Hagemann, S., Kuhry, P., Lafleur, P., Lee, H., Mazhitova, G., Nelson, F., Rinke, A., Romanovsky, V., Shiklomanov, N., Tarnocai, C., Venevsky, S., Vogel, J., and Zimov, S.: Vulnerability of permafrost carbon to climate change: implications for the global carbon cycle, Bioscience, 58, 701–714, 2008.
Sheffield, J., Goteti, G., and Wood, E. F.: Development of a 50 year high-resolution global dataset of meteorological forcings for land surface modeling, J. Climate, 19, 3088–3111, doi:10.1175/jcli3790.1, 2006.
Shen, C. and Phanikumar, M. S.: A process-based, distributed hydrologic model based on a large-scale method for surface-subsurface coupling, Adv. Water Resour., 33, 1524–1541, doi:10.1016/j.advwatres.2010.09.002, 2010.
Shevliakova, E., Pacala, S. W., Malyshev, S., Hurtt, G. C., Milly, P. C. D., Caspersen, J. P., Sentman, L. T., Fisk, J. P., Wirth, C., and Crevoisier, C.: Carbon cycling under 300 years of land use change: importance of the secondary vegetation sink, Global Biogeochem. Cy., 23, Gb2022, doi:10.1029/2007gb003176, 2009.
Stacke, T. and Hagemann, S.: Development and evaluation of a global dynamical wetlands extent scheme, Hydrol. Earth Syst. Sci., 16, 2915–2933, doi:10.5194/hess-16-2915-2012, 2012.
Stehman, S. V.: Selecting and interpreting measures of thematic classification accuracy, Remote Sens. Environ., 62, 77–89, doi:10.1016/s0034-4257(97)00083-7, 1997.

HESSD
11, 8443–8492, 2014

Subin, Z. M., Koven, C. D., Riley, W. J., Torn, M. S., Lawrence, D. M., and Swenson, S. C.: Effects of soil moisture on the responses of soil temperatures to climate change in cold regions, J. Climate, 26, 3139–3158, doi:10.1175/jcli-d-12-00305.1, 2013.

Sulman, B. N., Desai, A. R., Schroeder, N. M., Ricciuto, D., Barr, A., Richardson, A. D., Flanagan, L. B., Lafleur, P. M., Tian, H. Q., Chen, G. S., Grant, R. F., Poulter, B., Verbeeck, H., Ciais, P., Ringeval, B., Baker, I. T., Schaefer, K., Luo, Y. Q., and Weng, E. S.: Impact of hydrological variations on modeling of peatland CO_2 fluxes: results from the North American Carbon Program site synthesis, J. Geophys. Res., 117, G01031, doi:10.1029/2011JG001862, 2012.

Tian, W., Li, X., Cheng, G.-D., Wang, X.-S., and Hu, B. X.: Coupling a groundwater model with a land surface model to improve water and energy cycle simulation, Hydrol. Earth Syst. Sci., 16, 4707–4723, doi:10.5194/hess-16-4707-2012, 2012.

Todd-Brown, K. E. O., Randerson, J. T., Post, W. M., Hoffman, F. M., Tarnocai, C., Schuur, E. A. G., and Allison, S. D.: Causes of variation in soil carbon simulations from CMIP5 Earth system models and comparison with observations, Biogeosciences, 10, 1717–1736, doi:10.5194/bg-10-1717-2013, 2013.

Todd-Brown, K. E. O., Randerson, J. T., Hopkins, F., Arora, V., Hajima, T., Jones, C., Shevliakova, E., Tjiputra, J., Volodin, E., Wu, T., Zhang, Q., and Allison, S. D.: Changes in soil organic carbon storage predicted by Earth system models during the 21st century, Biogeosciences, 11, 2341–2356, doi:10.5194/bg-11-2341-2014, 2014.

Troch, P. A., Paniconi, C., and van Loon, E. E.: Hillslope-storage Boussinesq model for subsurface flow and variable source areas along complex hillslopes: 1. Formulation and characteristic response, Water Resour. Res., 39, 1316, doi:10.1029/2002wr001728, 2003.

Vergnes, J.-P. and Decharme, B.: A simple groundwater scheme in the TRIP river routing model: global off-line evaluation against GRACE terrestrial water storage estimates and observed river discharges, Hydrol. Earth Syst. Sci., 16, 3889–3908, doi:10.5194/hess-16-3889-2012, 2012.

Vergnes, J. P., Decharme, B., Alkama, R., Martin, E., Habets, F., and Douville, H.: A Simple Groundwater Scheme for Hydrological and Climate Applications: description and Offline Evaluation over France, J. Hydrometeorol., 13, 1149–1171, doi:10.1175/jhm-d-11-0149.1, 2012.

HESSD
11, 8443–8492, 2014

Walter, B. P. and Heimann, M.: A process-based, climate-sensitive model to derive methane emissions from natural wetlands: application to five wetland sites, sensitivity to model parameters, and climate, Global Biogeochem. Cy., 14, 745–765, 2000.

Weishampel, P., Kolka, R., and King, J. Y.: Carbon pools and productivity in a 1-km(2) heterogeneous forest and peatland mosaic in Minnesota, USA, Forest Ecol. Manag., 257, 747–754, doi:10.1016/j.foreco.2008.10.008, 2009.

Winter, T. C.: The concept of hydrologic landscapes, J. Am. Water Resour. As., 37, 335–349, doi:10.1111/j.1752-1688.2001.tb00973.x, 2001.

Wood, E. F., Roundy, J. K., Troy, T. J., van Beek, L. P. H., Bierkens, M. F. P., Blyth, E., de Roo, A., Doll, P., Ek, M., Famiglietti, J., Gochis, D., van de Giesen, N., Houser, P., Jaffe, P. R., Kollet, S., Lehner, B., Lettenmaier, D. P., Peters-Lidard, C., Sivapalan, M., Sheffield, J., Wade, A., and Whitehead, P.: Hyperresolution global land surface modeling: meeting a grand challenge for monitoring Earth's terrestrial water, Water Resour. Res., 47, W05301, doi:10.1029/2010wr010090, 2011.

Xie, Z. H., Di, Z. H., Luo, Z. D., and Ma, Q.: A Quasi-Three-Dimensional Variably Saturated Groundwater Flow Model for Climate Modeling, J. Hydrometeorol., 13, 27–46, doi:10.1175/jhm-d-10-05019.1, 2012.

Yu, Z. C.: Northern peatland carbon stocks and dynamics: a review, Biogeosciences, 9, 4071–4085, doi:10.5194/bg-9-4071-2012, 2012.

Yuan, X., Xie, Z. H., Zheng, J., Tian, X. J., and Yang, Z. L.: Effects of water table dynamics on regional climate: a case study over east Asian monsoon area, J. Geophys. Res., 113, D21112, doi:10.1029/2008jd010180, 2008.

Zhu, X., Zhuang, Q., Lu, X., and Song, L.: Spatial scale-dependent land–atmospheric methane exchanges in the northern high latitudes from 1993 to 2004, Biogeosciences, 11, 1693–1704, doi:10.5194/bg-11-1693-2014, 2014.

HESSD
11, 8443–8492, 2014

Table 1. Experimental design.

Simulation Name	Topographic Slope ζ	Soil-Depth Scale z_s (m)	Macropore Conductivity k_m (10^{-3} m s^{-1})	Hillslope Shape
Base	FAO[a]	3	0.1	Rectangular[b]
Untiled	FAO	3	0.1	Rectangular
ConstGeo[c]	0.1	3	0.1	Rectangular
HiMacro	FAO	3	1.0	Rectangular
ShalSoil	FAO	1	1.0	Rectangular
Concave	FAO	3	1.0	Concave
Converging	HWSD[d]	3	1.0	Converging
HWSDSlope	HWSD	1	1.0	Rectangular
HWSDSlopeBimodal	HWSD	1	1.0	2 hillslopes per gridcell
Untiled-CORPSE	FAO	3	1.0	Rectangular
CORPSE	FAO	3	0.1	Rectangular

[a] Topography from FAO/UNESCO (2003).
[b] i.e., linear profile shape and constant-width shape.
[c] This simulation included a constant topographic slope of 0.1, a constant soil texture of "medium" (Milly et al., 2014), and a constant bedrock hydraulic conductivity of 2×10^{-6} m s^{-1}.
[d] Topography from FAO/IIASA/ISRIC/ISSCAS/JRC (2012).

HESSD
11, 8443–8492, 2014

Table 2. Hydrology evaluation.

Simulation Name	Water Table Correlation[a]	Geometric-Mean Water-Table Depth	Wetland Area (10^6 km^2)	Wetland Area Correlation[b]	Wetland Sensitivity, Precision[b] (%)	Inundated Area (10^6 km^2)	Inundated Area Correlation[c]
Base	0.31	15	14.4	0.32	47, 20	10.6	0.18
Untiled	0.35	10	9.1	0.23	27, 17	6.5	0.18
ConstGeo	0.15	21	11.4	0.28	39, 22	9.3	0.18
HiMacro	0.38	21	3.0	0.30	18, 37	2.0	0.15
ShalSoil	0.29	15	7.4	0.30	30, 27	4.8	0.17
Concave	0.38	19	9.1	0.38	39, 27	6.6	0.22
Converging	0.38	22	2.9	0.30	19, 36	2.0	0.16
HWSDSlope	0.47	17	5.2	0.34	25, 35	3.3	0.16
HWSDSlopeBimodal	0.46	17	8.8	0.20	34, 21	9.4	0.18
Untiled-CORPSE	0.37	15	1.3	0.14	9, 22	1.5	0.07
CORPSE	0.31	15	15.3	0.32	48, 20	11.3	0.17
"Observed"		18[d]	6.2[e]			10.1[b]	

[a] With the log of the interpolated water-table depth from Fan et al. (2013), excluding permafrost gridcells diagnosed from each simulation.
[b] Compared to Lehner and Doll (2004), interpolated to the land-model grid.
[c] Compared to or from Papa et al. (2010), interpolated to the land-model grid.
[d] From Fan et al. (2013), interpolated to the land-model grid, excluding permafrost gridcells diagnosed from Base.
[e] From Lehner and Doll (2004), interpolated to the land-model grid. Note that the original, non-interpolated dataset contains 8.2–10.1 million km^2 of wetlands.

HESSD
11, 8443–8492, 2014

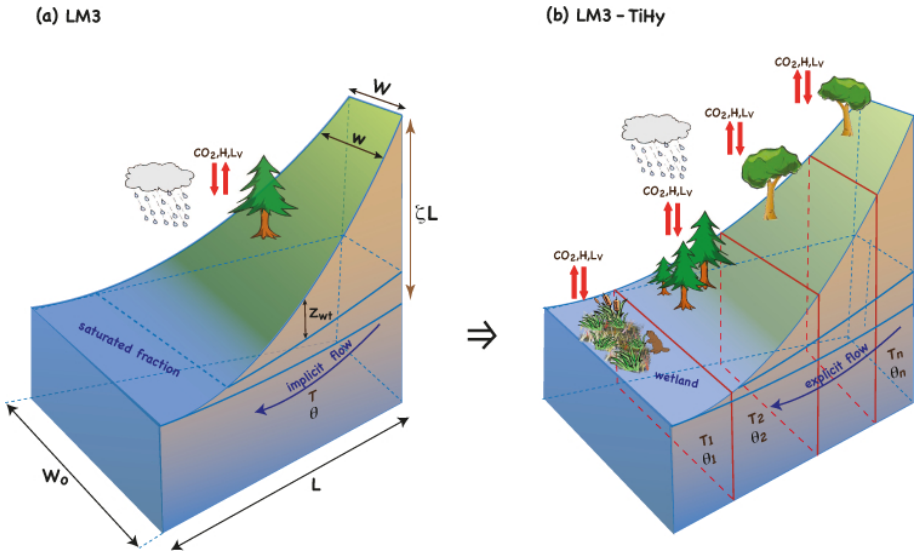

Figure 1. Hillslope Schematic. **(a)** Untiled LM3 (Milly et al., 2014); and **(b)** Tiled LM3-TiHy. T is temperature; Θ is soil water; w is hillslope width; $w_0 = 1$ and W are widths at the stream and hilltop, respectively; z_{wt} is water table depth; L is hillslope length; ζ is the hillslope slope (i.e., the ratio of the elevation at the hilltop to L); H is sensible heat flux; and L_v is latent heat flux.

HESSD
11, 8443–8492, 2014

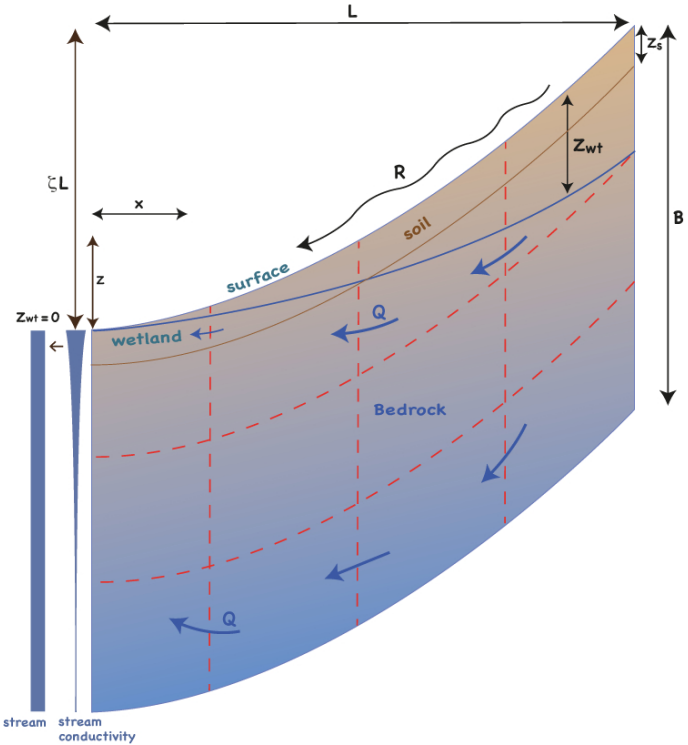

Figure 2. Discretized conceptual hillslope unit. Symbols are as in Fig. 1; additionally, z is the elevation above the stream; x is the horizontal distance along the hillslope from the stream; Z_s is the soil-depth scale; B is the domain thickness to the impermeable bottom; Q is the soil water flux; and R is the surface runoff. The stream is at constant hydraulic head.

HESSD
11, 8443–8492, 2014

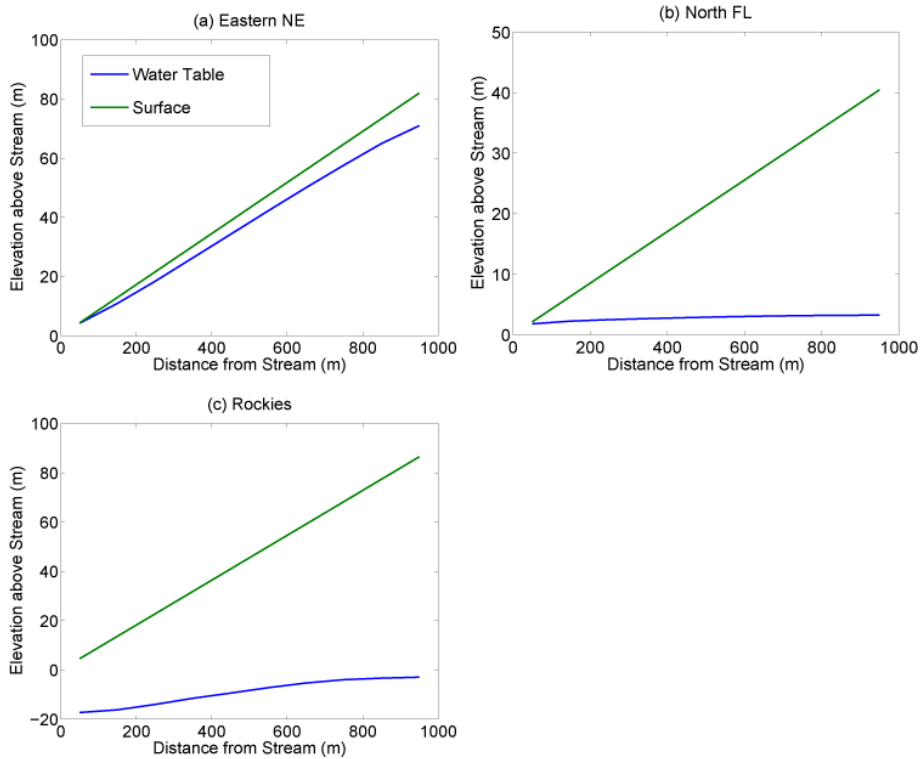

Figure 3. Three water table regimes. The water table profile in the Base simulation for selected gridcells, plotted with the local surface profile: **(a)** Eastern New England (43° N, −71° E); **(b)** North Florida (27° N, −81° E); and **(c)** the Colorado Rockies (39° N, −106° E).

HESSD
11, 8443–8492, 2014

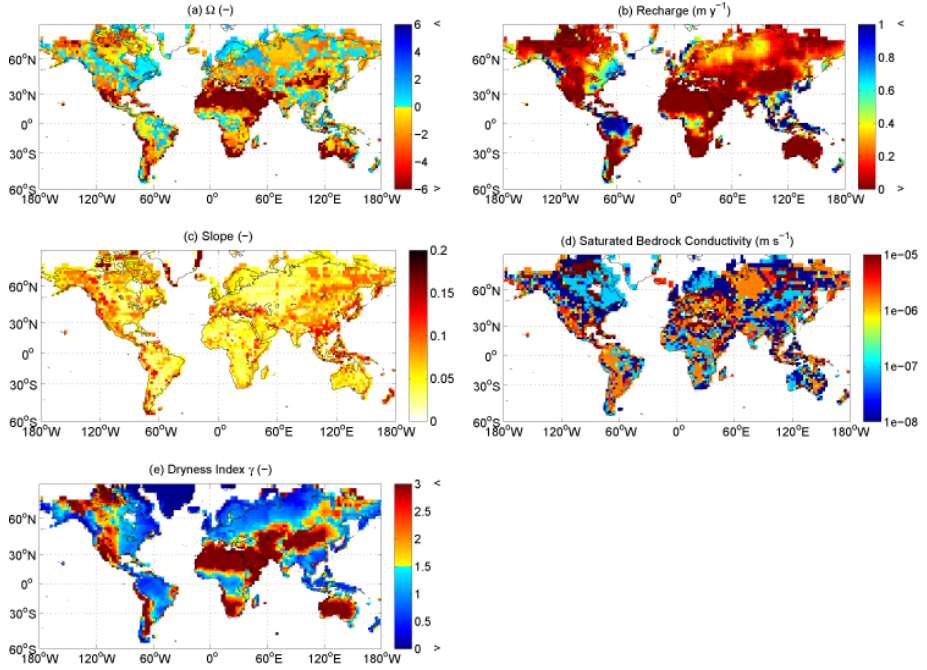

Figure 4. Water table determinants. Diagnostics from the Base simulation: **(a)** $\log_{10}$ of the water table ratio as defined in Gleeson et al. (2011a); **(b)** the runoff, computed as precipitation minus ET and restricted to be positive; **(c)** the prescribed topographic slope (FAO/UNESCO, 2003); **(d)** the saturated bedrock conductivity, interpolated from Gleeson et al. (2011b); and **(e)** the dryness index γ.

HESSD
11, 8443–8492, 2014

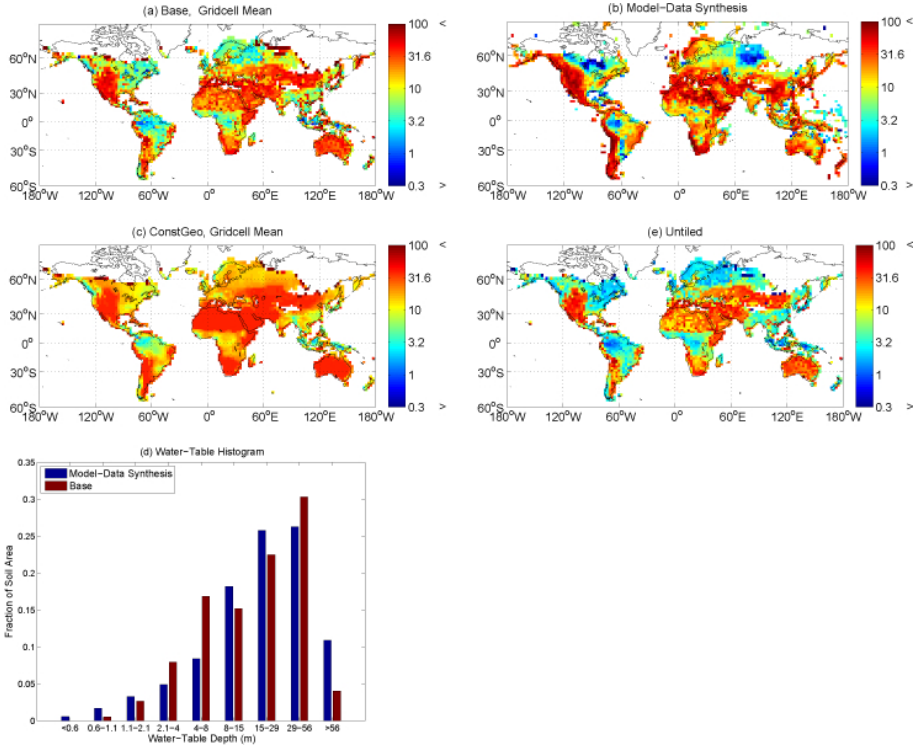

Figure 5. Global water table evaluation. Land-model gridcell-mean depth to water table (m) for: **(a)** the Base simulation; **(b)** Fan et al. (2013); **(c)** the ConstGeo simulation; and **(e)** the Untiled simulation. **(d)** Histogram comparing the gridcell-mean water-table area fractions for Fan et al. (2013) and the Base simulation.

HESSD
11, 8443–8492, 2014

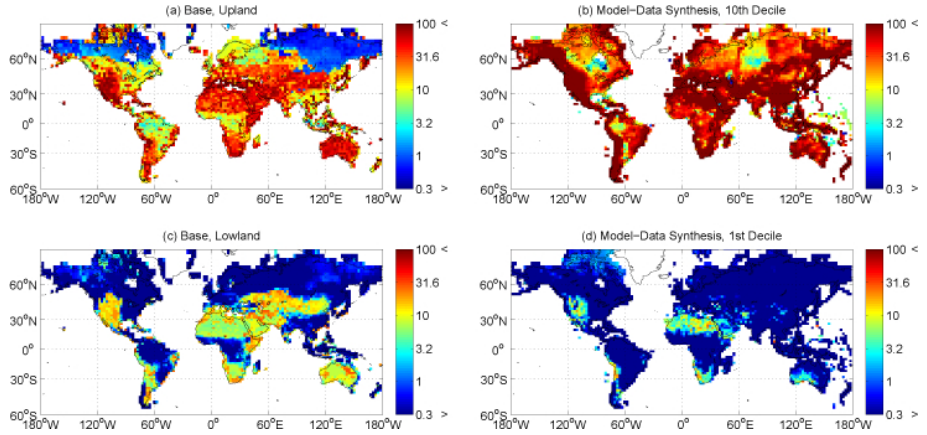

Figure 6. Upland and lowland water tables. Water-table depths (m) for: **(a)** the Base upland in each gridcell; **(b)** the tenth-decile depth in each land-model gridcell for Fan et al. (2013); **(c)** the Base lowland in each gridcell; and **(d)** the first-decile depth in each land-model gridcell for Fan et al. (2013).

HESSD
11, 8443–8492, 2014

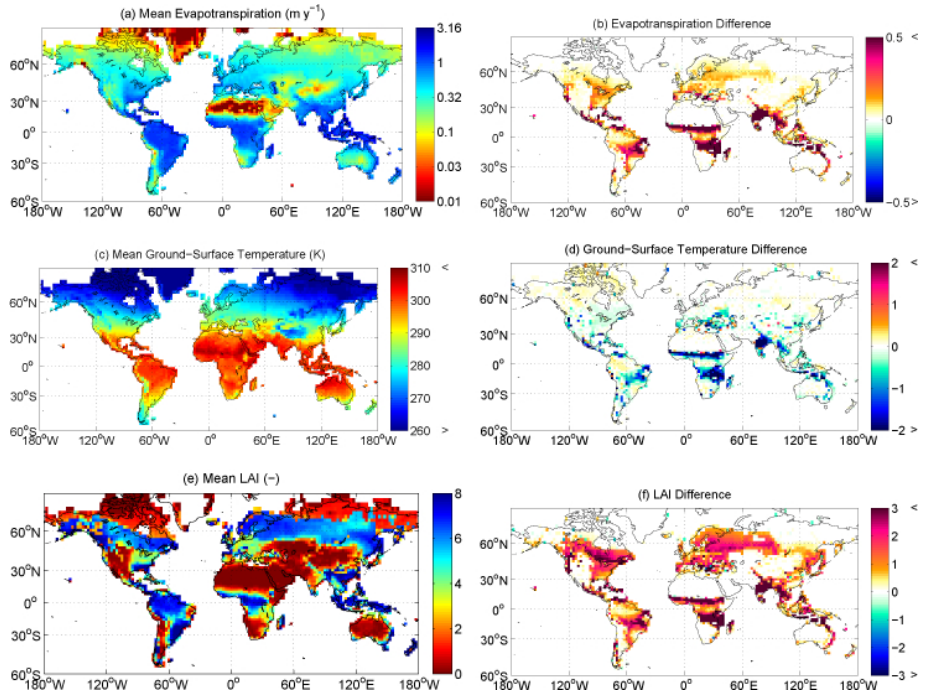

Figure 7. Global surface properties for the Base simulation: **(a)** mean ET; **(b)** the ET difference ($m\,yr^{-1}$) between the lowland and upland tiles; **(c)** mean ground-surface temperature; **(d)** the ground-surface temperature difference (K) between the lowland and upland; **(e)** mean LAI; and **(f)** the LAI difference between the lowland and upland.

HESSD
11, 8443–8492, 2014

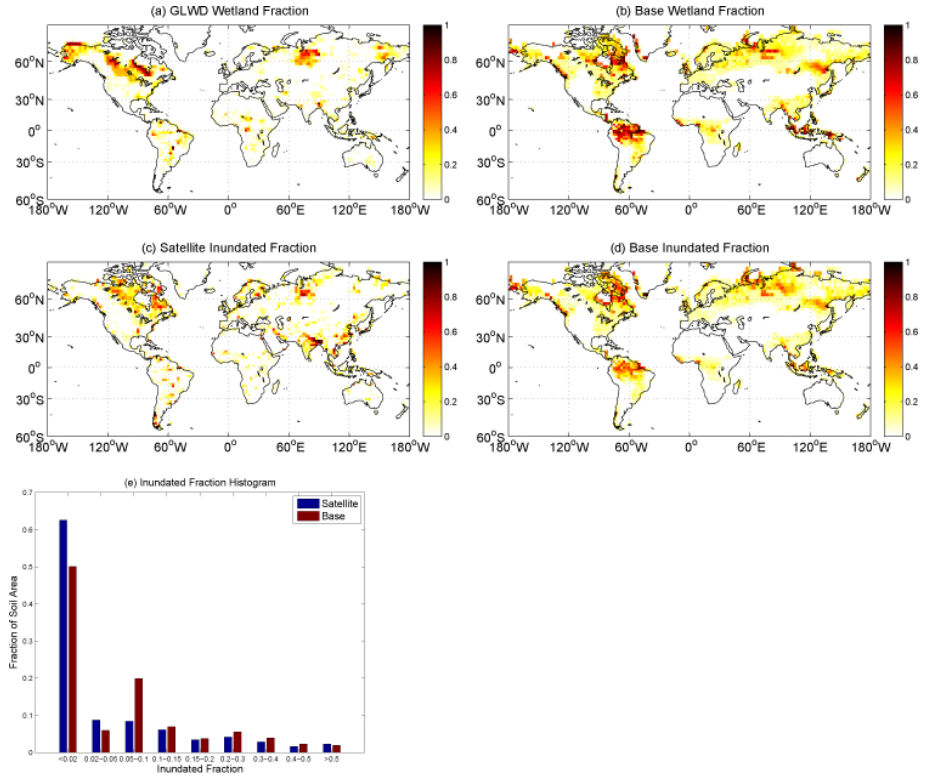

Figure 8. Wetland and inundated area extents. Wetland fraction for **(a)** the interpolated dataset of Lehner and Doll (2004); and **(b)** the Base simulation. Inundated area fraction for **(c)** the reconstruction of Papa et al. (2010); and **(d)** the Base simulation. **(e)** Histogram comparing the inundated area distribution for Papa et al. (2010) and the Base simulation.

HESSD
11, 8443–8492, 2014

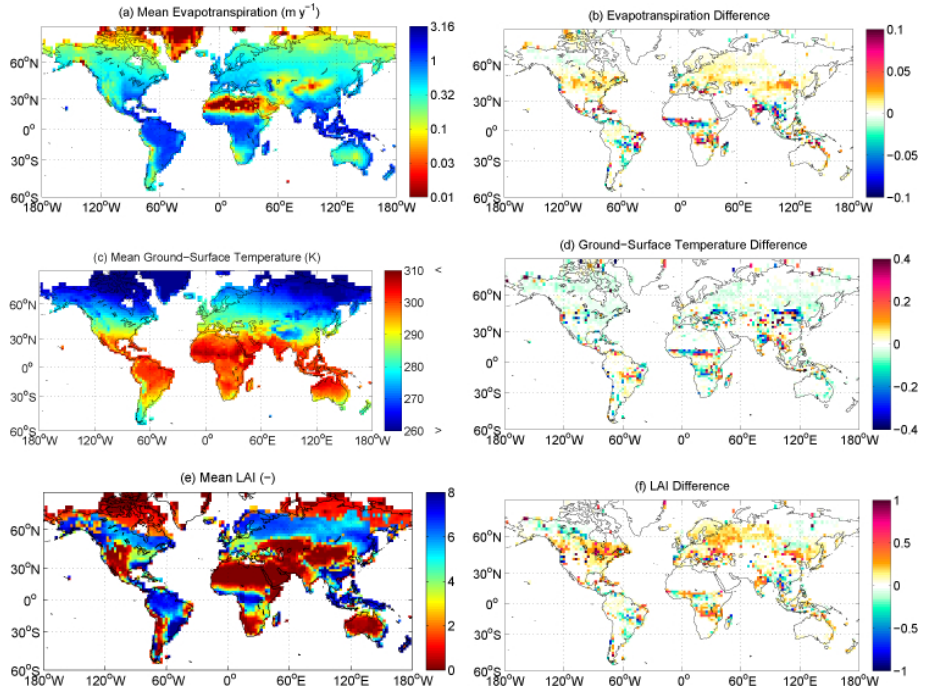

Figure 9. Comparison with Untiled simulation. **(a)** mean ET in Untiled; **(b)** the ET difference (m yr^{-1}) between the Base and Untiled simulations; **(c)** mean ground-surface temperature in Untiled; **(d)** the ground-surface temperature difference (K) between the Base and Untiled simulations; **(e)** mean LAI in Untiled; and **(f)** the LAI difference between the Base and Untiled simulations.

HESSD
11, 8443–8492, 2014

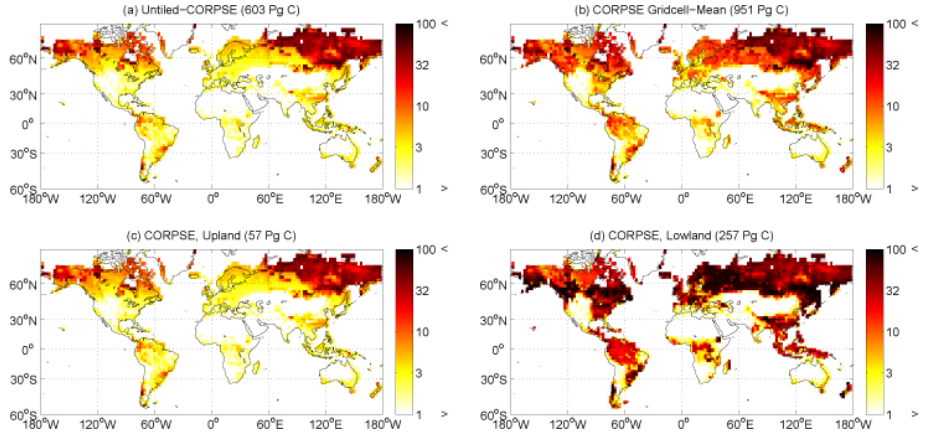

Figure 10. Soil carbon distributions. Total vertically-integrated soil carbon (kg C m^{-2}) for: **(a)** the Untiled-CORPSE simulation; **(b)** gridcell-mean for the CORPSE simulation; **(c)** the uplands (10 % of soil area) for the CORPSE simulation; and **(d)** the lowlands (10 % of soil area) for the CORPSE simulation.

HESSD
11, 8443–8492, 2014